New constraints from Central Chile on the origins of enriched continental compositions in thick-crusted arc magmas

Penny E. Wieser[1,2*], Stephen J. Turner[3], Tamsin A. Mather[1], David M. Pyle[1], Ivan P. Savov[4] and Gabriel Orozco[5]

[1] Department of Earth Sciences, University of Oxford, South Parks Road, Oxford OX1 3AN, UK

[2] Now at Department of Earth Sciences, University of Cambridge, Downing Street, Cambridge, UK, CB2 3EQ.

[3] Washington University in St. Louis, One Brookings Drive, St. Louis, MO 63130

[4] School of Earth and Environment, Institute of Geophysics & Tectonics, University of Leeds, Leeds LS2 9JT, UK.

[5] Red Nacional de Vigilancia Volcánica, Servicio Nacional de Geología y Minería, Av. Santa María 0104, Providencia, Chile.

* Corresponding author: pew26@cam.ac.uk. Phone: 07593670818

Abstract

Previous work has shown that arc volcanics from thick-crusted continental arcs are compositionally distinct from those erupted in island arcs or continental arcs with thinner crust (<30km). However, the relative influence of the slab, mantle, and upper plate on this variability remains poorly constrained. Subduction zones have been the loci of continental crust creation for over 2 Ga, so the

processes responsible for this variability have important implications for the chemical evolution of the Earth. The Andean Southern Volcanic Zone (SVZ; 33-46° S) is a particularly suitable setting in which to examine the mechanisms leading to enriched magma compositions in continental arcs, because both crustal thickness and magma chemistry vary consistently along strike. However, the scarcity of primitive samples from the northern SVZ, where the continental crust is thickest (50km), has precluded unbiased comparisons between the southernmost and northernmost volcanoes, and may have contributed to an overemphasis of the role of crustal processing in along-arc trends. This study investigates the geochemistry (major and trace element abundances, $^{87}Sr/^{86}Sr$ and $^{143}Nd/^{144}Nd$) of new samples from Don Casimiro and Maipo volcanoes, which lie within the Diamante-Maipo Caldera Complex of the northern SVZ. While evolved Diamante-Maipo samples show evidence for crustal assimilation, the trace element and isotopic enrichment of the primitive samples analysed in this study cannot result from crustal processing, because plausible basement lithologies are not uniformly enriched in all of the necessary elements. Recycling of certain crustal lithologies via subduction erosion could potentially generate the isotopic composition of the Diamante-Maipo magmas, but would result in highly irregular trace element patterns that are not observed in the lavas. We argue that the relative enrichment of the northern SVZ is best explained by the presence of an enriched ambient mantle component (similar to EM1-type ocean island basalts), superimposed on a northward decline in melt extent. Rather than crustal recycling, the EM1-like signatures in arc volcanics may arise from recycling of metasomatized subcontinental lithospheric mantle (M-SCLM). This hypothesis is consistent with the isotopic composition of M-SCLM melts across South America, as well as the isotopic compositions of samples from the Argentinian rear arc adjacent to and south of Diamante-Maipo. These rear-arc centres not only corroborate the findings at the arc front, they also demonstrate extensive variability in the supply of slab fluids to regions well behind the arc. Our results caution that if ambient mantle enrichment

is not taken into account, petrogenetic models of evolved lavas may exaggerate the role of crustal assimilation, and models for the growth of continental crust may overestimate the amount of continental material that must be recycled back into the mantle to satisfy mass balance.

Key Words

- Mantle heterogeneity
- Andean Southern Volcanic Zone

Highlights

- NSVZ isotopic and trace element enrichment indicate an EM1-like mantle source.
- EM1-like signatures originate from recycling of M-SCLM from nearby cratons.
- Slab melting, low mantle melt extents, and M-SLCM may enrich continental arc lavas
- Slab fluids are not supplied vertically from their point of origin.

1. Introduction

Continental arc magmas, which erupt through thick over-riding crust, are compositionally distinct from oceanic arc magmas. They tend to have elevated incompatible element abundances, steeper incompatible trace element patterns (Fig. 1), and isotopic signatures offset to higher $^{87}Sr/^{86}Sr$ and lower $^{143}Nd/^{144}Nd$ than oceanic arc magmas (Leeman et al., 1983; Plank and Langmuir, 1988; Hildreth and Moorbath, 1988; Turner et al., 2015a; Farner and Lee, 2017). Many of these compositional characteristics correlate strongly with the thickness of the arc crust (Turner et al., 2015a), and have even been used as proxies to estimate changes in crustal thickness and rates of surface uplift though time (Profeta et al., 2015; Chiaradia, 2015; Chapman et al., 2015; Scott et al., 2018). Much of the compositional offset between thick and thin-crusted arcs can be accounted for

by higher extents of crystal fractionation and crustal assimilation in continental settings (e.g. Farner and Lee, 2017). However, some compositional differences persist even when considering volcanics that have not been extensively overprinted in the crust (e.g. Plank and Langmuir, 1988; Turner and Langmuir, 2015a; Turner et al., 2017; Schmidt and Jagoutz, 2017), which is suggestive of a mantle origin. Compositional differences among "primary" magmas from continental vs. oceanic settings have been attributed to variations in slab temperature (Ruscitto et al., 2012; Turner and Langmuir, 2015b; Schmidt and Jagoutz, 2017), different extents of mantle melting (e.g. Plank and Langmuir, 1988; Tormey et al., 1991; Turner et al., 2016), subduction erosion (e.g. Stern, 1989), or mantle heterogeneity that is not the direct result of subducting materials (e.g. Hickey et al., 1986; Ewart and Hawkesworth, 1987; Rogers and Hawkesworth, 1989; Hochstaedter et al., 2001; Pearce et al., 2007; Turner et al., 2017). Our understanding of the thermal structures of subducting plates, the growth of the continental crust, and the petrogenesis of evolved arc magmas depends critically on constraining the relative influence of each of these factors in producing the enriched compositions of continental arc magmas.

The Andean Southern Volcanic Zone (SVZ) is an excellent natural laboratory in which to investigate how the thick crusts and lithospheres of active compressional plate margins affect the compositions of magmas added to the continents. The SVZ (33-46° S) is one of four volcanically active segments within the Andean Cordillera, where the Nazca Plate subducts under South America. It is commonly subdivided into three segments: the northern, transitional, and southern SVZ (NSVZ, TSVZ and SSVZ respectively; Dungan et al., 2001; Fig. 2a). From the SSVZ to the NSVZ, crustal thickness increases from ~30-50 km (Fig. 2c), slab depth from 70-120 km (Tassara and Echaurren, 2012), the lower plate age from 16-37 Ma (at 42° S and 33° S respectively, Volker et al., 2011), and trench sediment thickness ranges from 1.3-2.1 km (c.f. Hildreth and Moorbath, 1991). There is also a well-

established geochemical gradient from the SSVZ to the NSVZ (Tormey et al., 1991; Hildreth and Moorbath, 1988; Hickey et al., 2016, Fig. 2d-e). Trace element abundances of SSVZ volcanoes, where the crust is thinnest, have similar trace element patterns, and fall within the compositional range of island arcs (Fig. 1). The scarcity of primitive lavas from the NSVZ, which overlies the thickest crust, has made it difficult for prior work to assess the chemical characteristics of NSVZ parental magmas, though an average of the more mafic TSVZ lavas ("Central Chile"; Turner and Langmuir, 2015a) indicates substantially higher trace element abundances, which are similar in character to the bulk continental crust and the average of the more mafic volcanics of Cascades stratovolcanoes (Fig. 1). Thus, the chemical variability between the SSVZ and NSVZ are analogous to the chemical offsets between island arcs and continental arcs.

While many prior studies have addressed the mechanisms producing along-strike compositional variability of the SVZ arc-front volcanoes (Lopez-Escobar et al., 1977; Hickey et al., 1986; Hildreth and Moorbath, 1988; Tormey et al., 1991; Jacques et al., 2014; Hickey et al., 2016), the role of enrichment and heterogeneity within the asthenospheric mantle feeding the arc has received relatively little attention. Such ambient mantle heterogeneity is commonly inferred from trace element and isotopic compositions of mid-oceanic ridge basalts (MORBs) and ocean island basalts (OIBs; Zindler and Hart, 1986; Willbold and Stracke, 2010). In OIBs, this variability can be accounted for by a handful of isotopically distinct end-member components, such as the "enriched mantle" end-members (EM1, EM2; e.g. Zindler and Hart, 1986), which are commonly modelled as the products of recycled lithospheric mantle, sediment, and ancient oceanic/continental crust (c.f. Willbold and Stracke, 2010). There is also evidence for ambient mantle heterogeneity in arcs, despite additional tectonic complexity. For example, a global compilation of samples from rear-arc provinces filtered to minimize slab contributions (Turner and Langmuir, 2015b) form a linear array,

extending to EM1-type OIB compositions, which are significantly more isotopically enriched (higher $^{87}Sr/^{86}Sr$ and lower $^{143}Nd/^{144}Nd$) than the average Depleted MORB Mantle (DMM; Fig. 3a). Models of corner flow find that rear-arc mantle domains are generally transported towards the arc-front. Therefore, this rear-arc data may indicate that ambient sub-arc mantle compositions also vary substantially (e.g. Woodhead et al., 2012). The Andean Southern Volcanic Zone (SVZ) rear arc exemplifies this enriched ambient mantle signature (Kay et al., 2013; Jacques et al. 2013, 2014; Søager et al., 2015a; Turner et al. 2017), with more enriched rear-arc $^{87}Sr/^{86}Sr$ and $^{143}Nd/^{144}Nd$ values than any other arc globally (Fig. 3a). A major goal of this work is thus to assess the relative influence of ambient mantle heterogeneity in a targeted region of the NSVZ.

This study investigates the petrogenesis of new mafic lava samples from the volcanoes Don Casimiro and Maipo within the Diamante-Maipo Caldera complex (34˚S, Fig. 2b), to better determine the geochemical character of NSVZ parental magmas. The lavas from Don Casimiro and the basal portion of Maipo are among the most primitive ever sampled within the NSVZ (Fig. 4a). This may be linked to their eruption immediately after the catastrophic formation (~150ka) of the Diamante Caldera (Orozco et al., 2015), prior to the re-organization and maturation of crustal magma reservoirs. These primitive NSVZ magma compositions allow us to characterise and explore the origins of magmatic enrichment within a thickened continental subduction zone.

This study also incorporates samples from seven Argentinean monogenetic cones, located up to 350 km behind the NSVZ arc front. This rear-arc volcanism initiated in the earliest Miocene, associated with a period of shallow slab subduction (Kay and Copeland, 2006). Steepening of the slab towards the present-day dip of 33° (Tassara and Echuarren, 2012) started at 5 Ma (Kay et al., 2005). The samples included in this study are from monogenetic cones that erupted within the last

1 Myr, after the cessation of slab steepening. The post-Miocene rear-arc volcanism may be due to the influx of hot asthenosphere during slab steepening from a Middle-Late Miocene flat slab regime (Ramos and Folguera, 2011), possibly in a mantle plume-like configuration (Burd et al., 2014). Regardless of the mode of magmagenesis, these samples provide additional constraints on the composition of the ambient sub-arc mantle beneath the SVZ, and enable examination of slab additions beyond the arc-front.

2. Samples and methods

Of the 15 arc-front samples studied (Fig. 4a-b), six represent the basal sequence of Maipo Volcano, the active stratovolcano at the centre of the Diamante-Maipo Caldera Complex (Fig. 2b). Nine were collected from Don Casimiro Volcano, a small eroded stratovolcano located ~10 km SW of Maipo with activity restricted to preglacial times (Charrier, 1979). $^{40}Ar/^{39}Ar$ dates indicate that early activity at these centres was contemporaneous (Orozco et al., 2015). All lavas contain ubiquitous olivine and clinopyroxene phenocrysts within a glassy groundmass. The more evolved samples also contain plagioclase, oxides, and orthopyroxene (details in SIA2). The rear-arc samples are from small monogenetic scoria cones (Fig. 2a). Olivine, clinopyroxene, and oxide phenocrysts dominate, with microcrysts of plagioclase and alkali feldspar, and minor apatite. Whole-rock major-element and trace-element analyses were conducted on all samples, with $^{87}Sr/^{86}Sr$ and $^{143}Nd/^{144}Nd$ data and olivine major and trace analyses also collected for a subset (methods in SIA3).

3. Results

The new Don Casimiro-Maipo samples are primitive calc-alkaline basaltic andesites to andesites and the rear-arc samples are primitive basalts-trachybasalts (Fig. 4a). Olivine phenocryst compositions

range from $Fo_{75.7}$-$Fo_{83.6}$ at the arc-front, and $Fo_{80.6}$-$Fo_{90.1}$ in the rear-arc (Appendix 3; Fig. SB1a). The olivine compositions of the three analysed arc-front samples and most rear-arc samples lie below the olivine – whole rock equilibrium line, indicating that minor olivine accumulation has occurred (up to 7 wt. %; Fig. SB1; Hickey et al., 2016).

The whole-rock Mg#s of Don Casimiro-Maipo samples mostly range from 60-70, indicating that these samples have undergone only minor crystal fractionation (Fig. 4a). There is little variation in SiO_2 (55.3-57.9 wt.%) within the sample set. Previous studies within the Diamante-Maipo Caldera (Hickey et al., 1986; Futa and Stern, 1988, Sruoga, 2005; Holm et al., 2014) have primarily sampled volcanics with significant europium anomalies ($Eu^* = [Sm_N \times Gd_N]^{0.5}$; Fig. 4b), indicating that samples have undergone fractionation of plagioclase or mixing between primitive and evolved magmas (e.g. Turner and Langmuir, 2015). In contrast, our higher Mg# samples have Eu/Eu*>0.9 (Fig. 4b).

Like most arc magmas, the mafic Don Casimiro-Maipo lavas and rear-arc scoria have high abundances of Cs, Rb, Ba, U, Th, Pb, and Sr relative to other elements of similar incompatibility during mantle melting, while Nb and Ta are relatively depleted (Fig. 1). The highly incompatible trace element abundances of the Don Casimiro-Maipo arc-front samples are elevated relative to typical mafic to intermediate samples from oceanic arcs or the SSVZ. Abundances in the rear-arc samples are generally even higher than the arc front. As noted by Holm et al. (2016), the rear-arc samples also have relative depletions in the high field strength elements Zr and Hf. The magnitude of this depletion is on the upper end of what is observed within the SVZ arc front, with Hf/Sm=~0.6. The Don Casimiro-Maipo samples, however, have smaller relative Zr-Hf depletions than any other primitive samples from the SVZ arc-front, with Hf/Sm=~0.8 (Fig. SB2). As noted by previous studies

(e.g. Hildreth and Moorbath, 1988), Don Casimiro-Maipo and NSVZ samples have lower Cs/Rb than Villarrica and other SSVZ samples.

Samples from Don Casimiro-Maipo have significantly more enriched isotope ratios (higher $^{87}Sr/^{86}Sr$ and lower $^{143}Nd/^{144}Nd$) than Villarrica and other mafic products from SVZ arc-front centres (Fig. 3b). The isotopic compositions of the most primitive Don Casimiro samples in this study generally have lower $^{87}Sr/^{86}Sr$ and higher $^{143}Nd/^{144}Nd$ than previously reported samples from the Diamante-Maipo caldera (Fig. 3b). The Maipo samples from this study lie at higher $^{87}Sr/^{86}Sr$ and lower $^{143}Nd/^{144}Nd$ than Don Casimiro Samples. The $^{87}Sr/^{86}Sr$ and $^{143}Nd/^{144}Nd$ of the rear-arc centres in this study fall between the literature SVZ data and Don Casimiro-Maipo.

4. Discussion

While the gradient of northerly-increasing crustal thickness in the SVZ theoretically provides the ideal setting to understand the relationship between primary magma compositions and crustal thickness, the scarcity of mafic lavas in the NSVZ has made prior assessment of the origin of geochemical variation difficult. The volcanological setting of early Don Casimiro-Maipo lavas allowed the magmas to rapidly ascend through the thick crust of the NSVZ and avoid extensive crystal fractionation. Samples from this unique geological setting can thus be used to improve our understanding of the relative contributions from crustal processing, mantle melting, slab fluxes, subduction erosion, and ambient mantle heterogeneity to the production of compositionally enriched magmas erupted from volcanoes in continental arcs.

212 4.1. Crustal processing at Don Casimiro-Maipo

213 When lavas from throughout the Diamante-Maipo caldera complex are considered, there is a clear
214 role for crustal assimilation or mixing during fractional crystallization (AFC). $^{87}Sr/^{86}Sr$ and
215 $^{143}Nd/^{144}Nd$ values correlate with indices of fractionation (Fig. SB3), and the assimilation of known
216 SVZ basement compositions can recreate the variation in trace element and isotope ratios between
217 the most primitive and most evolved samples (Fig. 4c-d).

218

219 Hildreth and Moorbath (1988) suggested that mantle-derived magmas are processed in a melting,
220 assimilation, storage, and homogenization (MASH) zone in the lower crust. In their model, mantle-
221 derived magmas throughout the SVZ initially have similar compositions, and the enriched
222 "baseline" composition of NSVZ magmas results from increased MASH processing due to the
223 thicker crust. Thus, the isotopic compositions of even the most primitive NSVZ volcanics would be
224 the result of mixing between SSVZ-like mantle melts and some crustal basement component.

225

226 It is not possible to conclusively determine whether the most primitive Don Casimiro-Maipo
227 samples are entirely free of crustal contamination. It is possible, however, to assess the plausibility
228 of a scenario in which the notable compositional differences between the more primitive magmas
229 of the SSVZ and NSVZ are the result of a MASH-like process. Villarrica volcano has a similar trace
230 element and isotopic composition to the other volcanoes of the SSVZ (Fig. 1, Fig. 3b), and has
231 erupted some of the most primitive magmas. For simplicity, an average composition of mafic
232 samples from Villarrica is used to represent the composition of SSVZ volcanics.

233

234 Crustal assimilation and mixing likely affect the evolved magmas of the Diamante Caldera (Sruoga
235 et al., 2005). Mixing between the primitive Don Casimiro-Maipo compositions and a set of sampled

crustal lithologies, for example, reproduces the chemical variability observed within the Diamante Caldera (Fig. 4c-d). While it is plausible that the evolved Diamante Caldera lavas can be related to the primitive Don Casimiro-Maipo lavas by a combination of assimilation and fractional crystallization, mixing between these same crustal rocks and primitive Villarrica samples *does not* reproduce the Don Casimiro-Maipo compositions (Fig. 4c-d). These assimilants produce rapidly decreasing K/Rb ratios prior to producing adequate enrichment in $^{87}Sr/^{86}Sr$, and none reach high enough Rb/Y. For the MASH model to explain the chemical differences between the NSVZ and SSVZ a lower-crustal assimilant distinct from that producing geochemical variability *within* the Diamante-Maipo caldera must be incorporated into Don Casimiro-Maipo primary magmas.

To test whether any plausible Andean crustal assimilant may be capable of bridging the compositional gap between Don Casimiro-Maipo and the SSVZ, the compositions of 348 basement outcrops and basement xenoliths from the SVZ and the surrounding area (22-46°S) were compiled (Lucassen et al. 2001; Lucassen et al., 2004 and others; Appendix 5), and mixed with the average composition of primitive Villarrica samples. Only 14% of potential assimilants produce mixed compositions within $^{87}Sr/^{86}Sr\pm 0.0001$ and $^{143}Nd/^{144}Nd\pm 0.00005$ of the primitive Don Casimiro-Maipo average (Fig. 5a). Of these isotopically plausible mixed compositions, only 35% have Eu anomalies within the range of the primitive Don Casimiro-Maipo samples ($Eu/Eu^*>0.9$). None of these mixed compositions have trace element signatures resembling Don Casimiro-Maipo (Fig. 5b). Incorporating crystal fractionation alongside assimilation cannot account for these compositional offsets, because the resulting compositions produce mismatches not only in overall elemental abundances but also in a variety of incompatible element ratios, and substantial fractional crystallization would rapidly drive down the magmatic Mg#.

It remains possible that the required MASH assimilant has evaded sampling within the Southern Andes. Consequently, it is worth considering what compositional characteristics a hypothetical assimilant must possess to bridge the compositional gap between the southern and northern SVZ. We assume a maximum of 20% assimilation, based on the relatively high Mg#s of primitive Don Casimiro-Maipo lavas (as assimilation drives cooling, and thus crystal fractionation; DePaolo, 1981). Given this, any suitable assimilant must have greater than ~450ppm Zr, ~1420ppm Sr, and ~0.63wt% P_2O_5. It is improbable that a crustal rock will possess these characteristics, because these elements typically become depleted, rather than enriched, during late stage crystal fractionation or crustal melting (e.g. Turner and Langmuir, 2015a). To illustrate this point, a compilation of all continental granites, diorites, syenites, and monzonites in the GEOROC database (N~3000 with trace element data) was searched for suitable assimilants (considering only trace element abundances). Only 15 samples possessed sufficient concentrations of Zr, Sr, and P_2O_5. Mixtures of these samples with the average primitive Villarrica composition have erratic trace element patterns, testament to the complex petrological histories of these unusually enriched lithologies. None recreate the observed trace element pattern of Don Casimiro-Maipo, particularly the negative Nb-Ta anomaly (Fig. 5c). Thus, although crustal assimilation is near pervasive among the samples of the NSVZ, and strongly influences the compositions of evolved samples in this region, attributing the compositional offset between the NSVZ and SSVZ to MASH processing is inconsistent with the available data from SVZ basement outcrops, as well as with fundamental considerations regarding the composition of the required assimilant.

The geochemistry of the northern-most rear-arc samples further reinforces the conclusion that the isotopic offset between NSVZ and SSVZ samples is not a product of MASH. Rear-arc $^{87}Sr/^{86}Sr$ and $^{143}Nd/^{144}Nd$ data fall along the “mantle array” (Fig. 3a; Søager et al., 2013; 2015a-b; Søager and

Holm, 2013; Kay et al., 2013; Jacques et al., 2013; 2014; Holm et al., 2014; Turner et al. 2017), which is difficult to recreate by assimilation of available basement (e.g. Fig. 5a). Additionally, rear-arc isotopic enrichment correlates with arc-front enrichment, despite substantial longitudinal offsets (Fig. 6a-b). This is difficult to reconcile with assimilation, as accretion and eastward migration of the arc-front since the Palaeozoic has produced a longitudinally fragmented basement, with different basement domains striking parallel to the coast (Kay et al., 2005). Assimilation of lithologies within these different basement domains would produce uncorrelated rear-arc and arc-front Sr and Nd isotope systematics and would be unlikely to generate the linear trend on Fig. 3a. Finally, even the most primitive northern rear-arc samples, which bear olivines in equilibrium with their whole-rock compositions and are nearly in equilibrium with the mantle (Fig. SB1), possess enriched trace element and isotopic signatures. It is improbable that such primitive samples have undergone substantial crustal overprinting of $^{87}Sr/^{86}Sr$ and $^{143}Nd/^{144}Nd$.

4.2 Assessing the slab and mantle melting contributions to SVZ compositional variation

The goal of this section is to determine to what extent slab components and melting processes contribute to the along-strike variability of SVZ volcanics. Volcanic trace-element abundances vary as a function of the extent of mantle melting (F) and residual mantle mineralogy. Highly incompatible elements, which partition preferentially into the melt phase, may have higher concentrations in the NSVZ due to lower F, rather than different mantle source abundances (Tormey et al., 1991). Lower F in the NSVZ may result from the thick northern lithosphere impinging on the mantle wedge (Turner et al., 2016). This would be consistent with the finding of lower F values in volcanic arcs with thicker crust globally (Plank and Langmuir, 1988; Turner and Langmuir, 2015b).

In addition to variability in F, the trace element compositions of primary arc magmas reflect the transportation of slab materials into the mantle wedge. To assess whether the compositions of both Villarrica and Don Casimiro-Maipo can be produced from a common ambient mantle composition with variable slab components and F, it is useful to consider the maximum solution space generated by these parameters alone. For these calculations, we assume slab melting, as the slab top temperatures for Central Chile (784˚C, D80 model of Syracuse et al., 2010) lie above the wet pelite and AOC solidi (Hermann and Spandler, 2007; Carter et al. 2015). Furthermore, the Syracuse et al. (2010) D80 values may represent minimum temperatures, given recent evidence for shear heating and shallower depths of slab-mantle coupling (Penniston-Dorland et al., 2015; England, 2018). Slab melt compositions were calculated by mixing the composition of subducted sediment (ODP1232; Turner et al., 2017) and MORB (Gale et al., 2013) in various proportions, following by melting using partition coefficients consistent with experimental values for slab melting at temperatures between 800-900 ˚C (SIA4.1; Kessel et al., 2005; Hermann and Rubatto, 2009; Skora and Blundy, 2010). These slab melts were then mixed with an estimate of the depleted MORB mantle composition (DMM; Workman and Hart, 2005). The composition of mantle melts derived from this mixed composition were calculated using experimentally-derived hydrous partition coefficients and melt reaction coefficients (model details in SIA4.1).

The resulting solution space is shown in Fig. 7a-b. The red area on Fig. 7a depicts the solutions made available by varying the proportions of slab components and melt extent. F=0.04 was chosen as the lowest plausible melt extent because F values <0.04 tend to produce alkali-basalt or silica undersaturated major element compositions (e.g. Baasner et al. 2016). Villarrica samples fall within this solution space (as do most SSVZ samples), and a model fit within this space (purple diamond) reproduces the entire suite of Villarrica incompatible trace elements (Fig. 8). While this model fit

does not represent a unique solution for Villarrica, it does demonstrate that a feasible quantitative solution exists that is consistent with available experimental constraints. In contrast, there is no solution for Don Casimiro-Maipo. Increasing the amount of sediment and AOC contributions to the depleted mantle source can recreate the high La/Sm ratios, but only at Sr/Nd values that are far too high (Fig. 7a). While reducing F shifts the melt composition to higher La/Sm, even at F=0.04 there is no possible match to the Don Casimiro-Maipo volcanics.

The composition of the slab components also varies as a function of slab temperature (Hermann and Rubatto, 2009). There are systematic changes in the slab age and depth beneath the SVZ arc front, with corresponding variations in the slab thermal parameter, Φ (Φ=slab age x convergence rate x sin(dip angle)). Therefore, one might expect hotter slab temperatures in the NSVZ. However, while the magnitude of geochemical variation in the SVZ comprises much of the compositional range seen among arcs globally, differences in Φ between the SSVZ and NSVZ are relatively minor on the global scale (Turner et al., 2016).

Certain aspects of the trace element differences between Don Casimiro-Maipo and Villarrica suggest subtle slab temperature variations are indeed present. Compared to Villarrica, Don Casimiro-Maipo has low Cs/Rb and high Hf/Sm (Fig. 1). These element pairs are not substantially fractionated from each other by mantle melting, so likely reflect differences in the mantle source composition. For these element ratios, it is plausible that observed mantle source variations are caused by higher slab temperature in the NSVZ. Cs is highly mobile in low temperature aqueous fluids, and may have been disproportionally lost during early slab dehydration (Savov et al., 2007; Spandler et al., 2007). A hotter slab temperature can also destabilize zircon during slab melting, producing the less pronounced Zr-Hf depletions at Don Casimiro-Maipo (e.g. Hirai et al., 2018). The

blue field on Fig. 7a shows the expansion of the available solution space for slab temperatures >900˚C, as calculated using the maximum measured experimental mobility of light rare earth elements (LREE) in slab melts. While the solution space shifts toward higher La/Sm at a given Sr/Nd, the mafic NSVZ volcanics still plot well outside of the realm of possible solutions. Despite evidence for differences in SVZ slab temperature, including a slab temperature parameter alongside variable F and varying slab proportions only increases the available solution space to the Red+Blue fields on fig. 7a, which clearly does not envelop the data from Don Casimiro-Maipo.

The same conclusion can be drawn from $^{87}Sr/^{86}Sr$ and $^{143}Nd/^{144}Nd$ (Fig. 7b). The isotopic solution space is simplified by the fact that these isotope ratios are not fractionated by melting. The pink field on Fig. 7b shows the solution space produced by variation in slab temperature and the proportions of slab melts. Again, the Don Casimiro-Maipo data falls well outside of the available solution space, because slab contributions predominantly drive wedge compositions to higher $^{87}Sr/^{86}Sr$ at near constant or increasing $^{143}Nd/^{144}Nd$.

4.3 Is there geochemical evidence for subduction erosion?

SVZ rear-arc volcanics form a linear array between MORB-like compositions and EM1-type OIBs in $^{87}Sr/^{86}Sr$ vs. $^{143}Nd/^{144}Nd$ space (Kay et al., 2013; Søager et al., 2015a; Fig. 3a), and both rear-arc and arc-front samples are characterized by similar along-strike variability in these isotopes (Fig. 6a-b). If the isotopic offset between the mafic NSVZ and SSVZ samples is neither a product of crustal assimilation nor variation in the slab component, some EM1-like contaminant must be introduced to the mantle source of the SVZ. The origins of EM1-type OIBs are debated, with suggestions including deep recycling of lower continental crust (LCC), pelagic sediment and oceanic crust, or metasomatized subcontinental lithospheric mantle (Willbold and Stracke, 2010). The first

suggestion is particularly apt in the SVZ, as it has been proposed that the NSVZ endured extensive subduction erosion (the removal of upper plate material via abrasion and plucking by the lower plate) throughout the Cenozoic (Stern, 1989). While the composition of the South Andean LCC is not well constrained, the possible compositions of this reservoir can be inferred from the ever-growing dataset of regional basement compositions (Appendix 5). Although these samples were collected from surface outcrops, such outcrops may be representative of deep crustal lithologies due to Miocene episodes of tectonic thickening and under-thrusting (Hildreth and Moorbath, 1991). Thus, this database likely represents lithologies within both the upper and lower crust, and can be used not only to test models of lower crustal recycling, but also recycling of the entire crustal column forming the outbound belt of the South American Plate vulnerable to subduction erosion, including the upper crust (as suggested by Holm et al., 2014; 2016).

To assess the subduction erosion hypothesis, basement compositions (Appendix 5) were mixed with the estimated composition of the Villarrica mantle source. Only 11% of the mixed compositions pass within $^{87}Sr/^{86}Sr \pm 0.0001$ and $^{143}Nd/^{144}Nd \pm 0.00005$ of the most primitive Don Casimiro-Maipo samples (Fig. 9a). Only 15% of the isotopically plausible mixed compositions have Eu anomalies within the range of the primitive Don Casimiro-Maipo samples ($Eu/Eu^* > 0.9$), none of which recreate the concentrations of Y, Gd, Sm, Sr, Ba and $^{87}Sr/^{86}Sr$ ratios (Fig. 9b-c). To conclude, no mixed compositions with adequate trace element data falls within the range of the Don Casimiro-Maipo for $^{87}Sr/^{86}Sr$, $^{143}Nd/^{144}Nd$, and trace element abundances.

While some studies in this region (e.g. Holm et al., 2014; 2016) have found that SVZ volcanic compositions can be related by subduction erosion of sampled crustal lithologies, our preceding analysis does not support this conclusion. This is possibly because the newly sampled Don Casimiro-

405 Maipo samples are more primitive, while those in previous studies were affected by plagioclase
406 fractionation, magma mixing, or crustal assimilation, which accounts for their lower Eu/Eu* values.
407 It is possible that limited basement exposure in the SVZ means that the appropriate mixing lithology
408 has avoided sampling, but regional considerations also indicate the LCC chemical model is
409 implausible. Willbold and Stracke (2010) provide a model by which EM1-like isotopic compositions
410 are produced by mixing LCC starting materials into normal MORB mantle. However, this model
411 assumes that the LCC domains in question have been extracted and isolated from the mantle for >4
412 Ga, while the Chilenia and Cuyania terranes comprising the lower crust of the NSVZ-TSVZ are only
413 of Grenvillian age (~1Ga; Ramos, 2010). Because of this relatively young age, the typical basement
414 of the Southern Andes has $^{143}Nd/^{144}Nd$ values that are too high (relative to $^{87}Sr/^{86}Sr$) to serve as an
415 appropriate end-member (see mixed compositions in Fig. 9a). When considering the full array of
416 available trace element abundances and isotope values, the subduction erosion hypothesis does
417 not appear to be consistent with the geochemical systematics, possibly indicating that the extent of
418 subduction erosion has been over-estimated for this region. For example, Stern (1989) estimated
419 erosion rates based on the assumption that the distance between the trench and the arc front
420 remained constant throughout the Miocene, while recent geophysical models find that arc-front
421 migration relative to trench location might be a common process (e.g. Karlstrom et al., 2014).
422 Alternatively, subduction erosion may have affected the Andean margin in the past, but the eroded
423 material has since been flushed from the mantle wedge by corner flow.
424
425 Rear-arc geochemical variability is also inconsistent with the subduction erosion hypothesis. Rear-
426 arc isotopic enrichment persists at distances exceeding 600 km from the trench; it seems unlikely
427 that material eroded at the trench could spread hundreds of kilometres in the opposite direction of
428 corner flow. It may instead be carried down with the subducting slab and released alongside other

slab inputs, but in this case the enriched signature would co-vary with other slab components. Instead, at 550 km from the trench rear-arc monogenetic samples have Ce/Pb values that range from 5 (similar to the arc front) to >20 (similar to MORBs; Fig. 10b), while rear-arc $^{143}Nd/^{144}Nd$ ratios are consistently enriched relative to DMM (Fig. 3a). Additionally, within a given latitude bracket rear-arc $^{143}Nd/^{144}Nd$ ratios have limited variability, and do not correlate significantly with Ce/Pb or other indices of slab addition. Finally, isotopic enrichment in both the rear arc and arc front increases in a reasonably symmetrical, coherent fashion on either side of a pronounced minima at 39° S (Fig. 6a-b; Turner et al., 2017). Although it has been suggested that subduction erosion increases northwards (Stern, 1989), this phenomenon cannot account for the increase in enrichment south of Villarrica. The spatial systematics of rear-arc compositions are therefore also inconsistent with subduction erosion.

4.4 EM1-type enrichment from a sub-continental lithospheric mantle source

An alternative source for the enriched EM1-like mantle signature of the NSVZ is Metasomatised Subcontinental Lithospheric Mantle (M-SCLM). The infiltration of low degree mantle melts (F~0.005) into the base of the lithospheric mantle produces enriched incompatible element concentrations, which rapidly evolve EM1-like isotopic compositions (McKenzie and O'Nions, 1995; Turner et al., 2017; Fig. 11). Additionally, M-SCLM provides a more homogenous end-member composition than crustally-derived materials (Rogers and Hawkesworth, 1989; Turner et al, 2017). This material may be stored for long periods in the lithospheric mantle until it is returned to the asthenosphere by delamination or erosion.

Field evidence supports the hypothesis that the SCLM surrounding the SVZ has EM1-like isotopic affinities. Three geographically separated suites of isotopically enriched igneous rocks across South America have been interpreted as direct melts of the enriched SCLM (see Fig. 2a):

1) Alkaline igneous rocks erupted near the edges of the Rio Apa-Luis Alves and Sao Franscisco Cratons (Gibson et al., 1995; 2005; Carlson et al., 1996).
2) Mesozoic metabasites from the Southern Rift (Lucassen et al., 2002).
3) Carboniferous granitoids from the Santo Domingo Complex of the Coastal Batholith (Parada et al., 1999).

The $^{87}Sr/^{86}Sr$ and $^{143}Nd/^{144}Nd$ of samples from these regions plot as a linear extension of the SVZ rear-arc array (Fig. 11) and cannot be accounted for by addition of variable slab components or assimilation of available basement. The remarkable alignment of these lithologies in isotopic space despite being geographically separated by hundreds to thousands of kilometres suggests that M-SCLM east and north of the SVZ has relatively homogeneous EM1 affinities. The isotopic trajectory of these SCLM melts is consistent with the expected isotopic evolution of SCLM enriched by low degree mantle melts (Turner et al., 2017; Fig. 11). In contrast, the field produced by addition of sampled basement lithologies to the mantle has higher $^{87}Sr/^{86}Sr$ at a given $^{143}Nd/^{144}Nd$ than the array of SCLM-melts and rear-arc volcanics. Additionally, the isotopic variability induced by basement contamination is significantly broader than the narrow trajectory of rear-arc and M-SCLM melts (grey field, Fig. 11).

The full trace element pattern of such low-degree, relatively high-pressure mantle melts is difficult to assess, as no appropriate partitioning experiment has been carried out. Instead, a compositional proxy can be calculated by inverting for the mantle source composition of Gough Island EM1-type OIB volcanics (Turner et al., 2017), where enrichment has been linked to deep recycling of SCLM

(Gibson et al., 2005). Trace element and isotopic ratios of the inverted source composition were subsequently adjusted within the limits of EM1-like ocean island basalts (Stracke et al. 2003; Willbold and Stracke, 2010) to produce a generic EM1 source (SIA4.2). By including EM1-like mantle heterogeneity as an additional parameter in the forward model, the solution spaces on Fig. 7a-b expands to include the green fields, which finally overlap the primitive Don Casimiro-Maipo trace element concentrations. Furthermore, a model fit was identified that is consistent with the full Don Casimiro-Maipo trace element and isotopic composition (Fig. 7-8). As with the model fit for Villarrica, the Don Casimiro-Maipo model does not represent a unique solution, but is a demonstration of the model's quantitative viability under combined evidence from field and experimental constraints.

The addition of M-SCLM to the mantle by erosion or delamination at the base of continental cratons behind the volcanic arc also provides a more consistent explanation for the spatial variability of both rear-arc and arc-front SVZ volcanic compositions. Turner et al. (2017) proposed two explanations for the gradual decline in isotopic enrichment towards a distinct minimum at 39°S (Fig. 6a-b). Firstly, they note the presence of a Permian terrane suture at 39° S (Rapalini et al., 2010). It is possible that M-SCLM was lost during rifting or subsequent collision between cratonic blocks (Fig. 12a). Secondly, a slab tear may be present at 200km depth on the lower plate at ~39° S (Pesicek et al., 2012). If M-SCLM is entrained equally throughout the SVZ, upwelling of depleted Pacific mantle (which has not interacted with M-SCLM) through this slab window could dilute the EM1 signature. The upwelling, depleted mantle would then spread northwards and southwards, perhaps aided by toroidal flow around the slab tear (Zandt and Humphreys, 2008), resulting in a gradual northward and southward increase in enrichment (Fig. 12b). This could also potentially explain the magnetotellurically imaged "plume" in the rear-arc (Burd et al., 2014). Geochemical

signatures associated with upwelling through a slab window in the Kula Volcanic Field (W. Anatolia, Turkey) are traced over >250km (Klaver et al., 2016), similar to the distances observed here.

4.5 The relationship between trace element heterogeneity and mantle mineralogy

If the geochemical differences between the NSVZ and SSVZ serve as an analog for the differences between thin and thick crusted arcs, then ambient mantle enrichment may be a common feature of continental arcs. Determining whether EM1-like signatures within the SVZ are characterized by a distinct mineralogy (peridotite vs. pyroxenite) thus has potential implications for melting reactions within these enriched mantle domains. It has been suggested that SVZ rear-arc EM1 signatures are held within pyroxenitic domains, and that a southward decrease in rear-arc olivine Mn/Fe values results from the presence of pyroxenite source lithologies beneath the southern rear-arc (Søager et al., 2015b; Brandt et al., 2017). However, $^{87}Sr/^{86}Sr$ and $^{143}Nd/^{144}Nd$ isotopes become *less* EM-1-like as Mn/Fe ratios decrease, which is difficult to reconcile with this interpretation (Fig. 13). Moreover, the samples presented in this study have some of the most enriched isotopic signatures in the rear arc, yet have olivine compositions traditionally associated with a peridotite source (Sobolev et al., 2007; Fig. SB4). This suggests that EM1 isotopic signatures are unrelated, or even anti-correlated to the amount of pyroxenite. Thus, although large pyroxenitic domains may be present in certain areas of the rear arc, the distribution of this material is an unlikely candidate to explain isotopic and trace element trends on the scale of the SVZ as a whole. Crucially, rear-arc isotopic ratios can be reproduced with ~2% addition of the inferred SCLM melts (e.g. Gibson et al. 1995; 2005) to the depleted mantle, which is unlikely to have a detectable influence on erupted olivine phenocryst chemistry. It is also worth considering whether olivine compositional classifications, which have been calibrated primarily for anhydrous ocean island basalts (e.g. Sobelov et al. 2007), can be robustly applied to hydrous systems (Wang et al., 2016). The detailed relationship between erupted

olivine compositions and mantle mineralogy in the SVZ, as well as the relationship between mantle mineralogy and general indices of mantle enrichment remains an exciting area of ongoing research.

4.6 Distribution of the slab components within the mantle

The geochemical characteristics of rear-arc centres not only reinforce the conclusions drawn at the arc-front regarding spatial trends in EM1-like enrichment, they also provide novel constraints on the spatial distribution of slab components beyond the arc front. Slab melts have high Th/Nb and Th/La, and low Ce/Pb, so these ratios serve as proxies for the extent to which slab components have infiltrated the mantle source of each monogenetic cone (Johnson and Plank, 1999; Plank, 2005). Remarkably, while slab-sensitive ratios generally decline with increasing trench distance, some cones retain elevated Th/La and Th/Nb and low Ce/Pb at nearly 600km from the trench (Fig. 10b).

Highly incompatible trace element ratios of rear-arc samples may also indicate the provenance of rear-arc slab components. Thermal models predict that slab-surface temperatures at SVZ rear-arc depths will be ~250° C higher than those under the arc front (Syracuse et al., 2010). Such high slab temperatures should lead to a relative reduction of zircon stability in the slab, whereas the rear-arc samples have Zr-Hf anomalies similar to those observed for the SSVZ arc-front (Hirai et al., 2018; Fig. SB2). This indicates that the slab component reaching the rear-arc mantle source may have been extracted from the slab at temperatures similar to the SSVZ arc-front slab component. Significant fractionation of other slab-derived elements would also be expected if slab components were extracted at temperatures ~250° C higher than at the arc-front. Th/La in slab melts may increase by ~25%, and Th/Nb and U/Nb by nearly an order of magnitude (Hermann and Rubatto, 2009), which would result in rear-arc and arc-front lavas with distinctly different mixing trajectories

for these trace elements. Instead, rear-arc and arc-front samples both lie on mixing lines between the arc-front slab melt composition and a mantle with varying amounts of EM1-like enrichment (Fig. 10a). These observations suggest that very little fractionation of these elements has occurred, which is most simply explained by similar slab top temperatures at the source of arc-front and rear-arc slab inputs.

The observation that rear-arc mantle sources 600 km from the trench appear to have been infiltrated by a slab component that is similar in composition to the arc-front slab component is surprising. It is conceivable that the rear-arc slab signatures represent remnant metasomatism of the mantle wedge from the period of Miocene shallow subduction. However, the samples of this study were probably erupted between 0.01-0.7 Ma (Folguera et al., 2009), 4-5 million years after the slab began to steepen. As the wedge will have "turned over" ~330km in this time, it is likely that Miocene slab inputs were effectively flushed from the asthenospheric sources of the rear-arc cones of this study. A more plausible explanation for both the abundance and composition of the slab fluxes in the rear-arc is that the slab components added to the sources of subduction volcanics are not derived from the slab directly beneath the sampled cone. Geophysical models demonstrate that mantle flow and compaction pressure gradients can affect the flow paths of materials separated from the slab (e.g. Cagnioncle et al., 2007; Wilson et al., 2014). Thus, the mantle source at the arc front may be influenced by slab components that have been extracted from the slab beyond the arc front, and the rear-arc mantle source may be supplied from small quantities of slab components transported in the opposite direction in regions of low porosity (Cerpa et al., 2017; Fig. 14b).

570 It also is possible that slab materials could be transported non-vertically by “mélange diapirs”.
571 However, recent experimental work (Cruz-Uribe et al., 2018) found that melts of such diapirs will
572 likely have >50 wt. % SiO_2, >18 wt. % Al_2O_3, and <8 wt. % MgO, while the most primitive SVZ rear-
573 arc basalts have >10 wt. % MgO, <48 wt. % SiO_2, and <15 wt. % Al_2O_3, as is typical of arc alkali
574 basalts generated by low degrees of melting from a lherzolite source (e.g. Baasner et al., 2016).
575 Additionally, the experimental mélange melts have positive Zr-Hf anomalies while the SVZ rear-arc
576 basalts have negative Zr-Hf anomalies (Fig. 1). We also find the possibility of a mélange diapir
577 ascending far above the slab surface without melting to be fundamentally implausible, given the
578 low wet solidus temperatures of sediments and altered ocean crust (Herman and Rubatto, 2009;
579 Carter et al., 2015). Thus, the geochemical systematics of SVZ rear-arc volcanics appear to be most
580 consistent with a strong role for slab melting followed by advective transport, compaction
581 channelling, down-dragging, and generally non-vertical transport of slab liquids through the mantle
582 wedge, consistent with recent numerical models of two-phase flow in the mantle wedge
583 (Cagnioncle et al., 2007; Wilson et al., 2014; Cerpa et al., 2017).
584
585 4.6 Implications for crustal growth and the thermal structure of the arc crust
586 The extent to which the compositions of continental arc volcanics are inherited from the mantle
587 rather than overprinted in the crust has important implications for models of crustal growth.
588 Abundances of highly incompatible trace elements in oceanic arcs are much lower than those of the
589 bulk continental crust (Fig. 1). If continental growth is driven primarily by the accretion of island
590 arcs, which have incompatible element abundances that are often an order of magnitude lower
591 those estimated for the bulk continental crust (Fig. 1), then the continental crust must represent
592 the result of extreme fractionation or remelting of this arc material, followed by recycling of >90%
593 of the initially emplaced magma back into the mantle. However, continental arc volcanism has also

contributed a substantial portion of the bulk material to the continental crust (Cao et al., 2017), and continental arc magmas have trace element patterns that more closely resemble the continents (Fig. 1). If this trace element enrichment is inherited from the mantle, then a substantially smaller amount of material must be returned to the mantle to account for the continental mass balance, possibly closer to 50% (Sisson and Kelemen, 2018). The differences between these two interpretations, in turn, have clear implications for the generation of large-scale mantle heterogeneity.

Evaluating the role of parental magma enrichment versus crustal overprinting is also critical to understanding the petrogenesis of differentiated arc magmas. If one assumes that an evolved arc magma with an "enriched" isotopic composition originated from a "depleted" mantle source similar to MORB, or that the mantle source has a uniform isotopic composition, they will reasonably infer that the enriched magma is composed largely of recycled crustal material and that isotopic variability among magmas is mostly driven by crustal recycling (e.g. Davidson et al., 1990; Luccasen et al., 2006). If instead one assumes that the mantle source is enriched and heterogeneous, then the inferred proportion of the crustal component in the erupted magma will be smaller. For example if the mantle source is assumed to be isotopically similar to typical MORBs, a mixing exercise such as that shown in Fig. 5 indicates that an average of 40% crustal assimilation is necessary to account for the erupted $^{87}Sr/^{86}Sr$ and $^{143}Nd/^{144}Nd$ values at Don Casimiro-Maipo. Instead, by invoking an enriched mantle source, we have found that these samples are potentially free of crustal contamination. The magnitude and variability of crustal assimilation and crustal melting have clear implications for our understanding of the thermal structures of volcanic arcs (e.g. Annen and Blundy, 2006).

5. Conclusions

The volcanic products of thick-crusted continental arcs have substantially higher abundances of incompatible trace elements, and more "enriched" isotopic signatures than island arcs. The origin of these enriched signatures has profound implications for the formation of the continental crust and the petrogenesis of evolved magmas. The Andean Southern Volcanic Zone (SVZ) is an ideal natural laboratory for investigating the role of crustal thickness in magma petrogenesis, because along-strike trends in SVZ crustal thickness and magma chemistry are analogous to the salient differences between island arcs and continental arcs. While primitive basaltic lavas are common in the Southern SVZ, mafic magmas are scarce in the Northern SVZ, which has made it difficult to distinguish between crustal and mantle signatures. The trace element and isotopic measurements of new Northern SVZ mafic lava samples from Don Casimiro-Maipo presented in this study provide valuable new constraints on these problems.

While it has been suggested that the geochemical offset between the northern and southern SVZ is primarily driven by the assimilation of continental crust, the addition of known SVZ basement lithologies to a melt composition characteristic of the Southern SVZ fails to recreate the enriched isotopic and trace element signatures of these new Don Casimiro-Maipo samples. Most mixed compositions have $^{87}Sr/^{86}Sr$ values that are too high at a given $^{143}Nd/^{144}Nd$, and none have appropriate trace element patterns. Moreover, no plutonic lithology sampled *globally* is sufficiently enriched in the required suite of trace elements, due to the fractionation of accessory phases such as zircon and apatite. Assimilation of these variably enriched lithologies produces erratic trace element patterns, dissimilar to those observed at Don Casimiro-Maipo. Simulating the process of subduction erosion by addition of crustal lithologies to a SSVZ-like mantle source also fails to

641 account for northern enrichment, as the resulting melt compositions display similarly unsuitable
642 isotopic systematics and erratic trace element patterns.
643
644 Variable melt extents arising from the northwards impingement of the upper plate on the mantle
645 wedge likely contribute to the observed trace element variability, but cannot account for the large
646 isotopic differences. Similarly, although trace element and isotopic differences in the slab
647 components of the SSVZ and NSVZ may arise due to differing slab temperatures or proportions of
648 slab components, the solution space made available by these parameters, even in combination,
649 does not encompass the trace element or isotopic compositions of mafic Don-Casimiro Maipo
650 samples.
651
652 Thus, the compositions of primitive Don Casimiro-Maipo lavas appear to require not only the
653 addition of slab melts to the mantle wedge and low degrees of mantle melting, but also an enriched
654 northern SVZ mantle source *prior* to slab metasomatism. This is evident from the fact that no other
655 mechanism can successfully reproduce the compositions of the northern SVZ volcanics.
656 Additionally, rear-arc magmas filtered to only include samples with minimal slab contributions
657 extend along the “mantle array” towards compositions similar to EM1-type OIBs. Finally, the most
658 enriched rear-arc samples lie behind the northern SVZ, with a clear decrease in enrichment
659 southwards towards the SSVZ. A forward model based on an inversion for an EM1-like mantle
660 source can successfully reproduce the isotopic composition and trace element composition of Don-
661 Casimiro Maipo, demonstrating that this interpretation is consistent with available experimental
662 constraints.
663

664 The isotopic trajectory of the rear-arc lavas is co-linear with other South American lavas that are
665 thought to be melts of metasomatized sub-continental lithospheric mantle (M-SCLM). Thus, a
666 plausible origin of the enriched mantle source within the SVZ is the addition of M-SCLM material to
667 the mantle wedge by erosion or delamination from the cratonic lithosphere behind the arc. The
668 presence of significant isotopic enrichment >600km “upstream” of the trench is more consistent
669 with an M-SCLM origin than subduction erosion. While the systematic along and across-arc
670 geochemical variations are difficult to reconcile with assimilation or subduction erosion of
671 regionally variable basement lithologies, the composition of the M-SCLM appears to be relatively
672 homogenous across a large area of South America. Variable mantle enrichment within the SVZ may
673 result from upwelling of depleted mantle through a slab tear or the absence of M-SCLM domains
674 around a paleosuture zone.
675
676 Our new data from the northernmost rear-arc province show that in addition to chemical variability
677 induced by variable M-SCLM addition to the mantle source, some rear-arc cones have highly
678 variable slab inputs that are surprisingly similar in composition to the arc front. This supports recent
679 two-phase flow models indicating non-vertical transport of slab materials (Cagnioncle et al., 2007;
680 Wilson et al., 2014; Cerpa et al., 2017).
681
682 This results of this study imply that the enriched trace element and isotopic compositions of
683 primitive lavas in the thick-crusted NSVZ are produced by low degree melting of an enriched
684 ambient mantle that is metasomatized by slab melts, rather than fractionation and crustal
685 assimilation. The similarities between the trace element enrichments of these primitive NSVZ and
686 the bulk continental crust (Fig. 1) suggests that these mantle processes may play a major role in the
687 origin of enriched continental compositions globally. An important avenue of future research is to

688 constrain the extent to which the processes leading to enrichment in the NSVZ are applicable to
689 thick crusted arcs elsewhere. This will require revaluation of enriched signatures in the most
690 primitive lavas of other thick crusted arcs (e.g. Cascades, Mexico, Guatemala, Colombia). If
691 similarities with the SVZ are found, they will provide valuable constraints on models of continental
692 crust generation and elemental cycling within the silicate earth. For example, if ambient mantle
693 heterogeneity contributes substantially to enriched continental compositions, continental mass
694 balances require smaller amounts of material to be returned to the mantle.
695
696 Acknowledgments
697 The authors acknowledge NERC grant 'Mantle volatiles: processes, reservoirs and fluxes'
698 (NE/M000427/1) for funding, Melissa Murphy for help with clean lab chemistry, Sally Gibson for use
699 of the LA-ICP-MS, Jason Day for helping with analysis, and Patrick Sugden for assistance with
700 sample preparation for Sr and Nd isotopes in Leeds.
701
702

703 Figure Captions
704
705 Fig. 1– Trace element Signatures. Trace elements at Don Casimiro-Maipo (this study) are highly
706 enriched compared with Villarrica and the majority of oceanic arcs, and show slight enrichment
707 over the Cascades and Central Chile (Turner et al., 2016). The trace element pattern is similar to the
708 bulk continental crust (Rudnick and Gao, 2003). Don Casimiro-Maipo shows extreme HREE
709 depletion, indicating abundant garnet in the source mantle. Villarrica shows a very similar trace
710 element signature to other SSVZ centers (Llaima, Puyehue and Osorno are shown here; Turner et al.

711 2016), justifying its use as the SSVZ end-member in the modelling of this study. Rear-arc samples
712 show distinctive arc-like signatures, and even greater enrichment than Don Casimiro-Maipo. Spider
713 diagrams normalized to Pyrolite, McDonough and Sun, (1995).
714
715 Fig. 2-Geographical context and sample locations. a) Map of the SVZ, with segment boundaries
716 defined by Dungan et al. (2001). The location of arc-front volcanoes with primitive samples, and the
717 rear-arc sample locations of this study and the GEOROC database are shown. The locations of
718 inferred M-SCLM melts in Fig. 11 are also shown. Basemap from GEOMAP APP. b) Sample locations
719 of Don Casimiro and Basal Maipo lavas within the Diamante-Maipo Caldera Complex. Imagery from
720 Google Earth. c) Moho depth versus projected latitude within the SVZ. Moho depth is calculated at
721 each volcanic centre south of Don Casimiro-Maipo in a) from Tassara and Echaurren (2012).
722 Projected latitude is calculated by projecting a GPS co-ordinate along the convergence vector of the
723 Nazca plate to the Chile trench (Turner et al., 2017). d) and e) Major and trace element
724 concentrations in primitive samples (Turner et al. 2016 and this study) increase northwards,
725 mirroring changes in crustal thickness.
726
727 Fig. 3- Isotopic and trace element variability within the Andean SVZ placed within a global context.
728 a) Literature SVZ rear-arc samples filtered to remove high slab inputs (Th/Nb<0.4) fall on a mantle
729 array between DMM and EM1-type ocean island basalts, greatly extending the variability observed
730 globally in rear-arc provinces (rear-arc averages from Turner et al., 2017). Fields are drawn
731 incorporating EM1 and EM2-type ocean island basalts from Stracke et al. (2003). Literature values
732 from Don Casimiro-Maipo lie at the enriched end of this field with respect to global rear-arc
733 variability. The isotopic end-members used for modelling are shown. The EM1 model isotopic
734 composition is taken from a sample from Pitcairn (57DS9; Stracke et al., 2003), which falls near the

735 enriched end of EM1-type ocean island basalts. The depleted end member, Baseline Andean
736 Mantle (BAM), was chosen to plot at the depleted end of the rear-arc array (Sample 126171 from
737 Søager et al., 2013). The Nazca Plate sediment composition is calculated from ODP1232 (Turner et
738 al., 2017). b) Don Casimiro and Maipo samples from this study show significantly more enriched
739 isotopic compositions than other SVZ arc-front centres (Turner et al., 2016). Villarrica lies at the
740 depleted end of the SVZ arc-front array. Within the Diamante-Maipo caldera, more evolved
741 samples from Don Casimiro and Maipo plot alongside literature data, following a shallower
742 trajectory than that separating Don Casimiro and Villarrica.
743
744 Fig. 4-Sample Characteristics. a) Don Casimiro-Maipo samples from this study are primitive basaltic
745 andesites. These samples significantly extend the number of primitive analyses available for this
746 centre. Circled samples are believed to have undergone olivine addition (Fig. SB1). Rear-arc samples
747 are primitive basalts-trachybasalts. b) Eu anomalies are negligible in the most primitive samples of
748 this study (>0.9), whereas the majority of literature samples show substantial anomalies. Eu/Eu*
749 was calculated with $Eu^* = (Sm_N \times Gd_N)^{0.5}$ or with $Eu^{**} = (Sm^2 \times Tb)^{1/3}$ where no Gd data was reported.
750 In both cases, element concentrations are normalized to CI chondrite (McDonough and Sun, 1995).
751 c-d) Assimilation of eight SVZ basement sample into primitive Don Casimiro-Maipo samples
752 produce mixing lines that encompass the isotopic and trace element chemical diversity within the
753 Diamante Caldera (from Lucassen et al. 2001; 84-31-1, 84-31-2, 84-42-1, 84-42-11, and Lucassen et
754 al. 2004; 00-77, 00-55, 00-58 and 00-05; lithologies chosen as they best recreate the variability
755 within the Diamante-Maipo caldera). However, assimilation of the same 8 samples cannot recreate
756 the separation between Don Casimiro-Maipo and Villarrica (grey lines). Models originate from the
757 primitive average of Don Casimiro-Maipo and Villarrica samples. Error bars in c) show ±1σ of the
758 variation among primitive samples.

759

760 Fig. 5-Testing crustal assimilation models. a) Isotopic mixing lines produced by assimilation of 348
761 crustal lithologies thought to be representative of SVZ basement (compiled from GEOROC and
762 other sources) into the average composition of primitive Villarrica samples. Only a small proportion
763 pass near Don Casimiro-Maipo. b) Trace element patterns of the mixed compositions that produce
764 isotopic ratios close to Don Casimiro-Maipo (red lines in a), and have Eu/Eu*>0.9. c) Mixed
765 compositions for the small subset of the ~3000 plutonic rocks from GEOROC that have sufficient
766 concentrations of Zr, Sr and P_2O_5 to recreate the enrichment of these elements at Don Casimiro-
767 Maipo. Mixed compositions were calculated for the % mixing required to recreate Zr
768 concentrations. All produce erratic trace element patterns, with none recreating the distinctive Nb-
769 Ta enrichment at Don Casimiro-Maipo.

770

771 Fig. 6 - Across and along-arc variation in rear-arc isotopes. a-b) Rear-arc isotopic ratios form
772 latitudinally coherent trends, with statistically significant R^2 values ($p<0.005$). A pronounced
773 minimum in $^{87}Sr/^{86}Sr$, and a maximum in $^{143}Nd/^{144}Nd$ is observed at ~39° S, with a reasonably linear
774 and symmetric decrease to the north and south. Rear-arc samples from this study fit within the
775 regional trends. Arc-front centres lie close to the rear-arc best fit line, showing that these spatial
776 trends in enrichment are also present at the arc-front. The deviation in $^{143}Nd/^{144}Nd$ between the
777 rear-arc and the arc-front south of 39° S likely results from the sparse sampling of rear-arc centres,
778 making it difficult to resolve regional trends from local variations in heterogeneity. This difference
779 may also reflect much smaller slab input to the rear-arc than arc-front

780

781 Fig. 7 – Trace element and isotopic solution space produced by varying the composition of slab
782 melts, the extent of melting, and the composition of the ambient mantle. a) The red field

783 represents the maximum solution space available by the addition of varying slab melt compositions
784 (up to 2% sediment melt, 10% AOC melt) to a depleted mantle ("baseline ambient mantle" (BAM),
785 with a trace element composition of DMM, and isotopic composition of Sample 126171; Søager et
786 al., 2013) melted at F=0.04-0.3. The blue field represents the additional solution space made
787 available by an increase in slab temperature (with a change in the partition coefficients of La, Sm,
788 and Nd; see SIA4.1). The green field represents the additional solution space made available by
789 mixing in various proportions of an EM1-like mantle source to BAM. b) The pink field represents the
790 solution space made available by varying the proportion of AOC and sediment, and the total
791 amount of slab melt, as well as slab temperature. The latter has a much smaller effect than in a),
792 hence the red and blue fields are combined for simplicity. As in a), the green field shows the
793 additional solution space made available by increasing enrichment. In both figures, it is clear that
794 only increasing EM1-like enrichment can recreate the composition at Don Casimiro-Maipo. The
795 diamonds represent the best model fits for Villarrica (F=0.1, 7.5% slab addition consisting of 17%
796 sediment, with no enrichment) and Don Casimiro-Maipo (F=0.056, 7.5% slab addition consisting of
797 23% sediment, with 80% EM1 enrichment). The full trace element signatures of these models are
798 shown in Fig. 8.
799
800 Fig. 8 – Trace element modelling results. The trace element composition of Villarrica can be well
801 matched at F=0.1 with addition of 7.5% slab melt consisting of 17% sediment. The extreme trace
802 element enrichment at Don Casimiro-Maipo is best recreated by addition of 80% enriched source,
803 and slight changes in the composition of the slab addition (23% AOC vs. 17% at Villarrica). The solid
804 black lines in both figures represents the best model fit for each centre at the enrichment and
805 proportions of AOC:SED mentioned above using low temperature slab partition coefficients. This
806 provides the best match for Villarrica. The dashed grey lines represent the model fit for each centre

807 at increased slab temperatures, assuming 70% loss of Cs in the forearc. This provides the best
808 model match for Don Casimiro-Maipo. Model envelopes are produced by adding and subtracting 1σ
809 of 33 measurements of ODP1232 (Turner et al., 2017). Melting conditions generated directly from
810 the physical modelling results of Turner et al. (2016).
811
812 Fig. 9– Modelling contamination of the mantle source by subduction erosion. a) Isotope systematics
813 of contamination of the Villarrica mantle source by subduction erosion. The isotopic composition of
814 the Villarrica mantle source was calculated from the Villarrica primitive average. Only a small
815 percentage of mixing lines pass near Don Casimiro-Maipo. b-c) Trace element and isotopic
816 signatures of the mixed compositions that produce isotopic ratios close to Don Casimiro-Maipo (red
817 lines in a), and have Eu/Eu*>0.9. The trace element composition of the Villarrica mantle source
818 was calculated from the best model fit in Fig. 8. None of these lithologies can recreate Sr, Ba and
819 $^{87}Sr/^{86}Sr$ systematics at Don Casimiro-Maipo. Error bars show 1σ of primitive samples at Don
820 Casimiro-Maipo and Villarrica based on 5 and 3 analyses respectively.
821
822 Fig. 10- Variation in rear-arc slab inputs. a) Mixing models of slab-sensitive ratios between a melt of
823 a rear-arc mantle source (F=0.02, melting at 3.3Gpa) that has not received slab inputs, and a melt of
824 a rear-arc mantle source at the same conditions that has received slab inputs (20% sediment, 80%
825 AOC). The orange wedge reflects progressive mixing of 10% slab (with ODP1232± 1σ) into a mantle
826 source with 0% EM1 enrichment, and the green wedge reflects mixing of 17% slab (with ODP1232±
827 1σ) into a mantle source with 80% EM1 enrichment. Rear-arc trace element ratios follow these
828 mixing lines remarkably closely, with the small amount of scatter likely explained by variable
829 conditions of melting along the rear-arc. b) Trace element ratios sensitive to slab additions versus
830 trench distance. MORB-OIB like values (red bar) start to appear at distances greater than 425km.

Remarkably high, arc-like ratios are seen up to 600km from the trench, with large scatter in ratios at large trench distances, contrary to the narrow range of observed isotopes.

Fig. 11 –Isotopic compositions of inferred SCLM melts within South America (approximate locations on Fig. 2a). These clearly extend the array that passes from DMM/DAM through the arc-front and rear-arc, to Don Casimiro-Maipo. The field produced by contaminating the Villarrica mantle source with crustal lithologies (Fig. 9a) is also overlain. This follows a much shallower trajectory than SCLM melts, and is significantly broader than the SCLM field. Mobile belt M-SCLM melts represent alkaline volcanics erupted on the edges of the Sao Fransisco craton and the Rio Apa-Luis Alves craton on the east coast of South America (Gibson et al., 1995; 2005 and Carlson et al., 1996). Southern Rift melts were erupted just north of the NSVZ (Lucassen et al., 2002). Carboniferous granitoids are from the Santo Domingo Complex of the Coastal Batholith (Parada et al., 1999). All are suggested to have sampled M-SCLM. The green and blue lines show a recycling model in which low degree melts are extracted from the depleted mantle (Salters and Stracke, 2004) and then aged for up to 2 Ga using the parameters from Stracke et al. (2003; c.f. Turner et al., 2017). A model with F=0.003-0.008 encapsulates the range of isotopic compositions observed in SCLM melts.

Fig. 12- Schematic diagrams showing possible explanations for the isotopic enrichment minimum, and its relationship to tectonic features. a) A Permian suture zone corresponds with an absence of M-SCLM. b) A slab tear allows depleted Pacific MORB mantle to upwell, and dilute the EM1-type enrichment above the tear. As the proportion of depleted Pacific MORB mantle declines northwards and southwards, isotopic signatures become more enriched. Upper plate geometry adapted from box model of Søager et al. (2015b), pp. 1514.

Fig. 13 – Assessing olivine chemistry alongside regional isotopic trends. Olivine Mn/Fe decreases southwards. However, over the same interval, there is a decrease in isotopic enrichment southwards. Literature values from Brandt et al. (2017), with rear-arc olivine compositions of this study overlain.

Fig. 14 – Schematic diagrams of rear-arc slab supply. a) Traditional model of slab supply, with buoyant rise of slab fluids to the rear-arc from a slab melting at higher pressure and temperature than at the arc-front. The composition of these fluids should change with increasing trench distance, as the depth to the slab increases. Additionally, at large trench distances, very little to no slab supply would be expected, due to the exhaustion of hydrous phases. b) Proposed model of this study, inspired by Cagniocle et al. (2007), Wilson et al. (2014) and Cerpa et al. (2017). Down dragging of fluids released at arc-front depths explains the similar composition of arc-front and rear-arc slab supply.

References

Annen, C., Blundy, J.D. and Sparks, R.S.J., 2006. The genesis of intermediate and silicic magmas in deep crustal hot zones. *Journal of Petrology*, **47(3)**, pp. 505-539.

Baasner, A., Médard, E., Laporte, D. and Hoffer, G., 2016. Partial melting of garnet lherzolite with water and carbon dioxide at 3 GPa using a new melt extraction technique: implications for intraplate magmatism. *Contributions to Mineralogy and Petrology*, **171(5)**, p.45.

878 Brandt, F.E., Holm, P.M. and Søager, N., 2017. South-to-north pyroxenite–peridotite source
879 variation correlated with an OIB-type to arc-type enrichment of magmas from the
880 Payenia backarc of the Andean Southern Volcanic Zone (SVZ). *Contributions to*
881 *Mineralogy and Petrology*, **172(1)**, pp. 1-25.
882
883 Burd, A.I., Booker, J.R., Mackie, R., Favetto, A. and Pomposiello, M.C., 2014. Three-dimensional
884 electrical conductivity in the mantle beneath the Payun Matru volcanic field in the
885 Andean backarc of Argentina near 36.5° S: evidence for decapitation of a mantle plume
886 by resurgent upper mantle shear during slab steepening. *Geophysical Journal*
887 *International*, **198**, pp. 812–827.
888
889 Cagnioncle, A.M., E. Parmentier, and L. T. Elkins-Tanton., 2007. Effect of solid flow above a
890 subducting slab on water distribution and melting at convergent plate boundaries.
891 *Journal of Geophysical Research*, **112 (B9).**
892
893 Cao, W., Lee, C.T.A. and Lackey, J.S., 2017. Episodic nature of continental arc activity since 750
894 Ma: A global compilation. *Earth and Planetary Science Letters*, **461, pp.85-95**.
895
896 Carlson, R.W., Esperanca, S. and Svisero, D.P., 1996. Chemical and Os isotopic study of
897 Cretaceous potassic rocks from southern Brazil. *Contributions to Mineralogy and*
898 *Petrology*, **125(4)**, pp.393-405.
899

Carter, L.B., Skora, S., Blundy, J.D., De Hoog, J.C.M. and Elliott, T., 2015. An experimental study of trace element fluxes from subducted oceanic crust. *Journal of Petrology*, **56(8)**, pp.1585-1606.

Cerpa, N.G., Wada, I. and Wilson, C., 2017. Fluid migration in the mantle wedge: Influence of mineral grain size and mantle compaction. *Journal of Geophysical Research: Solid Earth*, **122**, doi:10.1002/2017JB014046.

Chapman, J.B., Ducea, M.N., DeCelles, P.G. and Profeta, L., 2015. Tracking changes in crustal thickness during orogenic evolution with Sr/Y: An example from the North American Cordillera. *Geology*, **43(10)**, pp.919-922.

Charrier, R., 1979. Los Volcanes Andres y Don Casimiro: Dos centros descubiertos en los Andes entre 34° S Y 34° S 45' Latitud Sur. *Revista Geologica de Chile*, **8**, pp. 79–85.

Chiaradia, M., 2015. Crustal thickness control on Sr/Y signatures of recent arc magmas: an Earth scale perspective. *Scientific reports*, **5**, p.8115.

Cruz-Uribe, A.M., Marschall, H.R., Gaetani, G.A. and Le Roux, V., 2018. Generation of alkaline magmas in subduction zones by partial melting of mélange diapirs—An experimental study. *Geology*, **46(4)**, pp.343-346.

923 Davidson, J.P., McMillan, N.J., Moorbath, S., Wörner, G., Harmon, R.S. and Lopez-Escobar, L.,
924 1990. The Nevados de Payachata volcanic region (18 S/69 W, N. Chile) II. Evidence for
925 widespread crustal involvement in Andean magmatism. *Contributions to Mineralogy*
926 *and Petrology*, **105(4)**, pp.412-432.
927
928 DePaolo, D.J., 1981. Trace element and isotopic effects of combined wallrock assimilation and
929 fractional crystallization. *Earth and Planetary Science Letters*, **53(2)**, pp.189-202.
930
931 Dungan, M.A., Wulff, A. and Thompson, R., 2001. Eruptive stratigraphy of the Tatara–San
932 Pedro complex, 36 S, Southern Volcanic Zone, Chilean Andes: reconstruction method
933 and implications for magma evolution at long-lived arc volcanic centers. *Journal of*
934 *Petrology*, **42(3)**, pp.555-626.
935
936 England, P., 2018. On shear stresses, temperatures, and the maximum magnitudes of
937 earthquakes at convergent plate boundaries. *Journal of Geophysical Research*: Solid
938 Earth.
939
940 Ewart, A. and Hawkesworth, C.J., 1987. The Pleistocene-Recent Tonga-Kermadec arc lavas:
941 interpretation of new isotopic and rare earth data in terms of a depleted mantle source
942 model. *Journal of Petrology*, **28(3)**, pp.495-530.
943
944 Farner, M.J. and Lee, C.T.A., 2017. Effects of crustal thickness on magmatic differentiation in
945 subduction zone volcanism: A global study. *Earth and Planetary Science Letters*, **470**,
946 pp.96-107.

947

948 Folguera, A., Naranjo, J.A., Orihashi, Y., Sumino, H., Nagao, K., Polanco, E. and Ramos, V.A.,
949 2009. Retroarc volcanism in the northern San Rafael Block (34–35 30 S), southern
950 Central Andes: Occurrence, age, and tectonic setting. *Journal of Volcanology and*
951 *Geothermal Research*, **186(3)**, pp. 169-185.

952

953 Futa, K. and Stern, C.R., 1988. Sr and Nd isotopic and trace element compositions of
954 Quaternary volcanic centers of the southern Andes. *Earth and Planetary Science*
955 *Letters***, 88(3-4)**, pp.253-262.

956

957 Gale, A., Dalton, C. A., Langmuir, C. H., Su, Y. and Schilling, J. G., 2013. The Mean Composition
958 of Ocean Ridge Basalts*. Geochemistry, Geophysics, Geosystems*, **14(3)**, pp. 489–518.

959

960 Gibson, S. A., Thompson, R. N., Day, J. A., Humphris, S. E. and Dickin, A. P., 2005. Melt-
961 generation processes associated with the Tristan mantle plume: Constraints on the
962 origin of EM-1. *Earth and Planetary Science Letters*, **237(3–4)**, pp. 744–767.

963

964 Gibson, S. A., Thompson, R. N., Leonardos, O. H., Dickin, A. P., Mitchell, J. G., Paranaiba, A. and
965 Province, I., 1995. The Late Cretaceous Impact of the Trindade Mantle Plume : Evidence
966 from Magmatism in SE Brazil. *Journal of Petrology***, 36 (1)**, pp. 189-229.

967

968 Hermann, J. and Rubatto, D., 2009. Accessory phase control on the trace element signature of
969 sediment melts in subduction zones. *Chemical Geology*, **265(3–4)**, pp. 512–526.

970

971 Hermann, J. and Spandler, C.J., 2007. Sediment melts at sub-arc depths: an experimental
972 study. *Journal of Petrology*, **49(4)**, pp.717-740.
973
974 Hickey, R.L., Frey, F.A., Gerlach, D.C. and Lopez-Escobar, L., 1986. Multiple sources for basaltic
975 arc rocks from the southern volcanic zone of the Andes (34–41 S): trace element and
976 isotopic evidence for contributions from subducted oceanic crust, mantle, and
977 continental crust. *Journal of Geophysical Research: Solid Earth*, **91(B6)**, pp.5963-5983.
978
979 Hickey-Vargas, R., Holbik, S., Tormey, D., Frey, F.A. and Roa, H.M., 2016. Basaltic rocks from the
980 Andean Southern Volcanic Zone: Insights from the comparison of along-strike and
981 small-scale geochemical variations and their sources. *Lithos*, **258**, pp.115-132.
982
983 Hildreth, W. and Moorbath, S., 1988. Crustal contribution to arc magmatism in the Andes of
984 Central Chile. *Contributions to Mineralogy and Petrology*, **98**, pp. 455–489.
985
986 Hildreth, W. and Moorbath, S., 1991. Reply to Comment on "Crustal contributions to arc
987 magmatism in the Andes of Central Chile" by W. Hildreth and S. Moorbath.
988 *Contributions to Mineralogy and Petrology***, 108(1)**, pp. 247-252.
989
990 Hirai, Y., Yoshida, T., Okamura, S., Tamura, Y., Sakamoto, I. and Shinjo, R., 2018. Breakdown of
991 residual zircon in the Izu arc subducting slab during backarc rifting. *Geology*, **46(4)**,
992 pp.371-374.
993

994 Hochstaedter, A., Gill, J., Peters, R., Broughton, P., Holden, P. and Taylor, B., 2001. Across-arc
995 geochemical trends in the Izu-Bonin arc: Contributions from the subducting slab.
996 *Geochemistry, Geophysics, Geosystems*, **2(7)**, 2000GC000105.
997
998 Holm, P.M., Søager, N., Alfastsen, M. and Bertotto, G.W., 2016. Subduction zone mantle
999 enrichment by fluids and Zr–Hf-depleted crustal melts as indicated by backarc basalts of
1000 the Southern Volcanic Zone, Argentina. *Lithos*, **262**, pp. 135-152.
1001
1002 Holm, P.M., Søager, N., Dyhr, C.T. and Nielsen, M.R., 2014. Enrichments of the mantle sources
1003 beneath the Southern Volcanic Zone (Andes) by fluids and melts derived from abraded
1004 upper continental crust. *Contributions to Mineralogy and Petrology*, **167(5),** p.1004.
1005
1006 Jacques, G., Hoernle, K., Gill, J., Hauff, F., Wehrmann, H., Garbe-Schönberg, D., van den
1007 Bogaard, P., Bindeman, I. and Lara, L. E., 2013. Across-arc geochemical variations in the
1008 Southern Volcanic Zone, Chile (34.5-38.0° S): Constraints on mantle wedge and slab
1009 input compositions. *Geochimica et Cosmochimica Acta*, **123**, pp. 218–243.
1010
1011 Jacques, G., Hoernle, K., Gill, J., Wehrmann, H., Bindeman, I. and Lara, L. E., 2014. Geochemical
1012 variations in the Central Southern Volcanic Zone, Chile (38 – 43 ° S): The role of fluids
1013 in generating arc magmas. *Chemical Geology*, **371**, pp. 27–45.
1014
1015 Johnson, M. C., and Plank, T., 1999. Dehydration and melting experiments constrain the fate of
1016 subducted sediments. *Geochemistry, Geophysics, Geosystems*, **1(1)**, 1007,
1017 doi:10.1029/1999GC000014.

Karlstrom, L., Lee, C.T. and Manga, M., 2014. The role of magmatically driven lithospheric thickening on arc front migration. *Geochemistry, Geophysics, Geosystems*, **15(6)**, pp.2655-2675.

Kay, S.M. and Copeland, P., 2006. Early to middle Miocene backarc magmas of the Neuquén Basin: Geochemical consequences of slab shallowing and the westward drift of South America. *Geological Society of America Special Papers*, **407(9)**, pp. 185–213.

Kay, S.M., Godoy, E. and Kurtz, A., 2005. Episodic arc migration, crustal thickening, subduction erosion, and magmatism in the south-central Andes. *Bulletin of the Geological Society of America*, **117(1–2)**, pp. 67–88.

Kay, S.M., Jones, H.A. and Kay, R.W., 2013. Origin of Tertiary to Recent EM1 and subduction-like chemical and isotopic signatures in Auca Mahuida region (37-38S) and other Patagonian plateau lavas. *Contributions to Mineralogy and Petrology*, **166(1)**, pp. 165–192.

Kessel, R., Schmidt, M.W., Ulmer, P. and Pettke, T., 2005. Trace element signature of subduction-zone fluids, melts and supercritical liquids at 120–180 km depth. *Nature*, **437(7059)**, p.724.

Klaver, M., Davies, G.R. and Vroon, P.Z., 2016. Subslab mantle of African provenance infiltrating the Aegean mantle wedge. *Geology*, **44(5)**, pp. 367-370.

Leeman, W.P., 1983. The influence of crustal structure on compositions of subduction-related magmas. *Journal of Volcanology and Geothermal Research*, **18(1-4),** pp.561-588.

Lopez-Escobar, L., Frey, F.A. and Vergara, M., 1977. Andesites and high-alumina basalts from the central-south Chile High Andes: geochemical evidence bearing on their petrogenesis. *Contributions to Mineralogy and Petrology*, **63(3)**, pp.199-228.

Lucassen, F., Becchio, R., Harmon, R., Kasemann, S., Franz, G., Trumbull, R., Wilke, H., Romer, R. L. and Dulski, P., 2001. Composition and density model of the continental crust at an active continental margin — the Central Andes between 21 ° S and 27 ° S. *Tectonophysics,* **341(1)**, pp. 195–223.

Lucassen, F., Escayola, Æ. M., Romer, A. R. L., Kerstin, V. Æ. and Gerhard, K. Æ., 2002. Isotopic composition of Late Mesozoic basic and ultrabasic rocks from the Andes (23 – 32 ° S) – implications for the Andean mantle. *Contributions to Mineralogy and Petrology*, **143(3)** pp. 336–349.

Lucassen, F., Kramer, W., Bartsch, V., Wilke, H.G., Franz, G., Romer, R.L. and Dulski, P., 2006. Nd, Pb, and Sr isotope composition of juvenile magmatism in the Mesozoic large magmatic province of northern Chile (18–27 S): indications for a uniform subarc mantle. *Contributions to Mineralogy and Petrology***, 152(5)**, p.571.

Lucassen, F., Trumbull, R., Franz, G., Creixell, C., Vásquez, P., Romer, R. L. and Figueroa, O., 2004. Distinguishing crustal recycling and juvenile additions at active continental margins: The Paleozoic to recent compositional evolution of the Chilean Pacific margin (36-41° S). *Journal of South American Earth Sciences*, **17(2)**, pp. 103–119.

McDonough, W.F. and Sun, S.S., 1995. The composition of the Earth. *Chemical Geology*, **120**, pp. 223-253.

McKenzie, D.A.N. and O'Nions, R.K., 1995. The source regions of ocean island basalts. *Journal of Petrology*, **36(1)**, pp.133-159.

Orozco, G., Garces, F., Jara, G., and Lara, L.E., 2015. Nuevos antecedentes para la geología del complejo volcánico Maipo-Diamante, Andes del Sur. Congreso Geologico Chileno, La Serena, Octubre 2015. (abstract – accessed http://biblioteca.sernageomin.cl/opac/DataFiles/14905_v3_pp_218_221.pdf, 13th January, 2018).

Parada, M.A., Nyström, J.O. and Levi, B.., 1999. Multiple sources for the Coastal Batholith of central Chile (31–34 S): geochemical and Sr–Nd isotopic evidence and tectonic implications. *Lithos*, **46(3)**, pp.505-521.

Pearce, J.A., Kempton, P.D. and Gill, J.B., 2007. Hf–Nd evidence for the origin and distribution of mantle domains in the SW Pacific. *Earth and Planetary Science Letters*, **260(1)**, pp.98-114.

Penniston-Dorland, S.C., Kohn, M.J. and Manning, C.E., 2015. The global range of subduction zone thermal structures from exhumed blueschists and eclogites: Rocks are hotter than models. *Earth and Planetary Science Letters*, **428**, pp.243-254.

Pesicek, J. D., Engdahl, E. R., Thurber, C. H., Deshon, H. R. and Lange, D., 2012. Mantle subducting slab structure in the region of the 2010 M8.8 Maule earthquake (30-40° S), Chile. *Geophysical Journal International*, **191(1)**, pp. 317–324.

Plank, T. and Langmuir, C.H., 1988. An evaluation of the global variations in the major element chemistry of arc basalts. *Earth and Planetary Science Letters*, **90**, pp. 349–370.

Plank, T., 2005. Constraints from thorium/lanthanum on sediment recycling at subduction zones and the evolution of the continents. *Journal of Petrology*, **46(5)**, pp.921-944.

Profeta, L., Ducea, M.N., Chapman, J.B., Paterson, S.R., Gonzales, S.M.H., Kirsch, M., Petrescu, L. and DeCelles, P.G., 2015. Quantifying crustal thickness over time in magmatic arcs. *Scientific Reports*, **5**, p.17786.

Ramos, V.A., 2010. The Grenville-age basement of the Andes, *Journal of South American Earth Sciences*, **29**, pp. 77–91.

Ramos, V.A. and Folguera, A., 2011. Payenia volcanic province in the Southern Andes: An appraisal of an exceptional Quaternary tectonic setting. *Journal of Volcanology and Geothermal Research*, **201(1–4)**, pp. 53–64.

Rapalini, A.E., de Luchi, M.G.L., Dopico, C.M., Klinger, F.G.L., Giménez, M.E., Martínez, P., 2010. Did Patagonia collide with Gondwana in the Late Paleozoic? Some insights from a multidisciplinary study of magmatic units of the North Patagonian Massif. *Geologica Acta*, **8**, 349-371.

Rogers, G. and Hawkesworth, C.J., 1989. A geochemical traverse across the North Chilean Andes: evidence for crust generation from the mantle wedge. *Earth and Planetary Science Letters*, **91**, pp. 271-285.

Rudnick, R.L. and Gao, S., 2003. Composition of the continental crust. In: *Treatise on Geochemistry: The Crust* (Eds. R. Rudnick), **vol. 3**. Permagon, New York, pp. 1–64.

Ruscitto, D.M., Wallace, P.J., Cooper, L.B. and Plank, T., 2012. Global variations in H2O/Ce: 2. Relationships to arc magma geochemistry and volatile fluxes. *Geochemistry, Geophysics, Geosystems*, **13(3).**

Salters, V.J. and Stracke, A., 2004. Composition of the depleted mantle. *Geochemistry, Geophysics, Geosystems***, 5(5)**.

1135 Savov, I.P., Ryan, J.G., D'Antonio, M. and Fryer, P., 2007. Shallow slab fluid release across and
1136 along the Mariana arc-basin system: Insights from geochemistry of serpentinized
1137 peridotites from the Mariana fore arc. *Journal of Geophysical Research: Solid*
1138 *Earth*, **112(B9).**
1139
1140 Schmidt, M.W. and Jagoutz, O., 2017. The global systematics of primitive arc melts.
1141 *Geochemistry, Geophysics, Geosystems*, **18(8)**, pp.2817-2854.
1142
1143 Scott, E.M., Allen, M.B., Macpherson, C.G., McCaffrey, K.J., Davidson, J.P., Saville, C. and Ducea,
1144 M.N., 2018. Andean surface uplift constrained by radiogenic isotopes of arc
1145 lavas. *Nature Communications*, **9(1)**, p.969.
1146
1147 Sisson, T.W. and Kelemen, P.B., 2018. Near-solidus melts of MORB+ 4 wt% H 2 O at 0.8–2.8
1148 GPa applied to issues of subduction magmatism and continent formation. *Contributions*
1149 *to Mineralogy and Petrology*, **173(9)**, p.70.
1150
1151 Skora, S. and Blundy, J., 2010. High-pressure hydrous phase relations of radiolarian clay and
1152 implications for the involvement of subducted sediment in arc magmatism. *Journal of*
1153 *Petrology*, **51(11)**, pp.2211-2243.
1154
1155 Søager, N. and Holm, P.M., 2013. Melt-peridotite reactions in upwelling eclogite bodies:
1156 Constraints from EM1-type alkaline basalts in Payenia, Argentina. *Chemical Geology*,
1157 **360–361**, pp. 204–219.
1158

Søager, N., Holm, P.M. and Llambías, E.J., 2013. Payenia volcanic province, southern mendoza, argentina: OIB mantle upwelling in a backarc environment. *Chemical Geology*, **349–350**, pp. 36–53.

Søager, N., Martin, P. and Thirlwall, M.F., 2015a. Lithos Sr , Nd , Pb and Hf isotopic constraints on mantle sources and crustal contaminants in the Payenia volcanic province, Argentina. *Lithos*, **212–215**, pp. 368–378.

Søager, N., Portnyagin, M., Hoernle, K., Holm, P. M., Hauff, F. and Garbe-Schanberg, D., 2015b. Olivine major and trace element compositions in Southern Payenia Basalts, Argentina: Evidence for pyroxenite-peridotite melt mixing in a back-arc setting. *Journal of Petrology*, **56(8)**, pp. 1495–1518.

Sobolev, A. V., Hofmann, A. W., Kuzmin, D. V., Yaxley, G. M., Arndt, N. A., Chung, S.-L., Danyushevsky, L. V., Elliott, T., Frey, F. A., Garcia, M. O., Gurenko, A. A., Kamenetsky, V. S., Kerr, A. C., Krivolutskaya, N. A., Matvienkov, V. V., Nikogosian, I. K., Rocholl, A., Sigurdsson, I. A., Sushchevskaya, N. M. and Teklay, M., 2007. The amount of recycled crust in sources of mantle derived melts. *Science,* **316**, pp. 412–417.

Spandler, C., Mavrogenes, J. and Hermann, J., 2007. Experimental constraints on element mobility from subducted sediments using high-P synthetic fluid/melt inclusions. *Chemical Geology*, **239(3)**, pp.228-249.

1182 Sruoga, P., Llambías, E.J., Fauqué, L., Schonwandt, D. and Repol, D.G., 2005. Volcanological and
1183 geochemical evolution of the Diamante Caldera–Maipo volcano complex in the
1184 southern Andes of Argentina (34 10 S). *Journal of South American Earth Sciences*, **19(4)**,
1185 pp.399-414.
1186
1187 Stern, C.R., 1989. Pliocene to present migration of the volcanic front, Andean Southern
1188 Volcanic Zone. *Andean Geology*, **16(2)**, pp.145-162.
1189
1190 Stracke, A., Bizimis, M. and Salters, V.J., 2003. Recycling oceanic crust: Quantitative
1191 constraints. *Geochemistry, Geophysics, Geosystems*, **4(3).**
1192
1193 Syracuse, E. M., van Keken, P. E., Abers, G. A., Suetsugu, D., Bina, C., Inoue, T., Wiens, D. and
1194 Jellinek, M., 2010. The global range of subduction zone thermal models, *Physics of the*
1195 *Earth and Planetary Interiors*, **183(1–2)**, pp. 73–90.
1196
1197 Tassara, A. and Echaurren, A., 2012. Anatomy of the Andean subduction zone: Three-
1198 dimensional density model upgraded and compared against global-scale models.
1199 *Geophysical Journal International*, **189(1)**, pp. 161–168.
1200
1201 Tormey, D., Hickey-Vargas, R., Frey, F., Lopez-Escobar, L., 1991. Recent lavas from the Andean
1202 front (32 to 42° S); Interpretations of along-arc compositional variations. *Geological*
1203 *Society of America, Special Paper*, **265**, pp. 57–77.
1204

Turner, S.J. and Langmuir, C.H., 2015a. The global chemical systematics of arc front stratovolcanoes: Evaluating the role of crustal processes. *Earth and Planetary Science Letters*, **422**, pp.182-193.

Turner, S. J., and Langmuir, C. H., 2015b, What processes control the chemical compositions of arc front stratovolcanoes? *Geochemistry, Geophysics, Geosystems*, **16**, pp. 1865–1893.

Turner, S. J., Langmuir, C. H., Katz, R. F., Dungan, M. A. and Escrig, S., 2016. Parental arc magma compositions dominantly controlled by mantle-wedge thermal structure. *Nature Geoscience*, **9**, pp. 772-776,

Turner, S.J., Langmuir, C.H., Dungan, M.A. and Escrig, S., 2017. The importance of mantle wedge heterogeneity to subduction zone magmatism and the origin of EM1. *Earth and Planetary Science Letter*s, **472**, pp.216-228.

Völker, D., Kutterolf, S. and Wehrmann, H., 2011. Comparative mass balance of volcanic edifices at the southern volcanic zone of the Andes between 33 S and 46 S. *Journal of Volcanology and Geothermal Research*, **205(3-4)**, pp.114-129.

Wang, J., Li, L., Xiong, X., 2016. Trace Element Partitioning during Hydrous Mantle Melting and Source Mineralogy of Arc Basalts. *Goldschmidt Conference Abstracts*, **3322**.

Willbold, M. and Stracke, A. 2010. Formation of enriched mantle components by recycling of upper and lower continental crust. *Chemical Geology*, **276(3–4)**, pp. 188–197.

Wilson, C.R., Spiegelman, M., van Keken, P.E. and Hacker, B.R., 2014. Fluid flow in subduction zones: the role of solid rheology and compaction pressure. *Earth and Planetary Science Letters*, **401**, pp. 261–274.

Woodhead, J., Stern, R.J., Pearce, J., Hergt, J., Vervoort, J., 2012. Hf-Nd isotope variation in Mariana Trough basalts: The importance of "ambient mantle" in the interpretation of subduction zone magmas. *Geology*, **40**, pp. 539-542

Workman, R.K. and Hart, S.R., 2005. Major and trace element composition of the depleted MORB mantle (DMM). *Earth and Planetary Science Letters*, **231(1–2)**, pp. 53–72.

Zandt, G. and Humphreys, E., 2008. Toroidal mantle flow around the western US slab window. *Geology*, **36(4)**, pp. 295-298.

Zindler A., and Hart S., 1986. Chemical Geodynamics. *Annual Review of Earth Planetary Sciences*, **14**, pp. 493–571

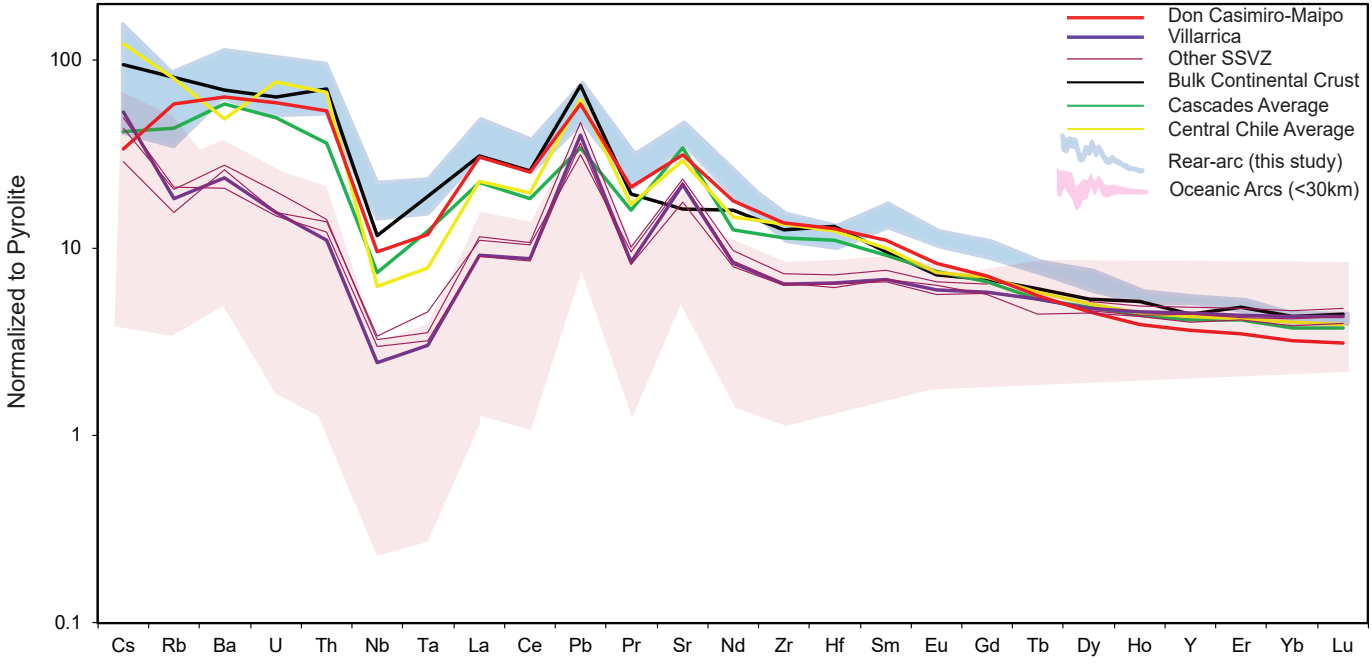
Normalized to Pyrolite
100
10
1
0.1
Cs
Rb
Ba
U
Th
Nb
Ta
La
Ce
Pb
Pr
Sr
Nd
Zr
Hf
Sm
Eu
Gd
Tb
Dy
Ho
Y
Er
Yb
Lu
Don Casimiro-Maipo
Villarrica
Other SSVZ
Bulk Continental Crust
Cascades Average
Central Chile Average
Rear-arc (this study)
Oceanic Arcs (<30km)

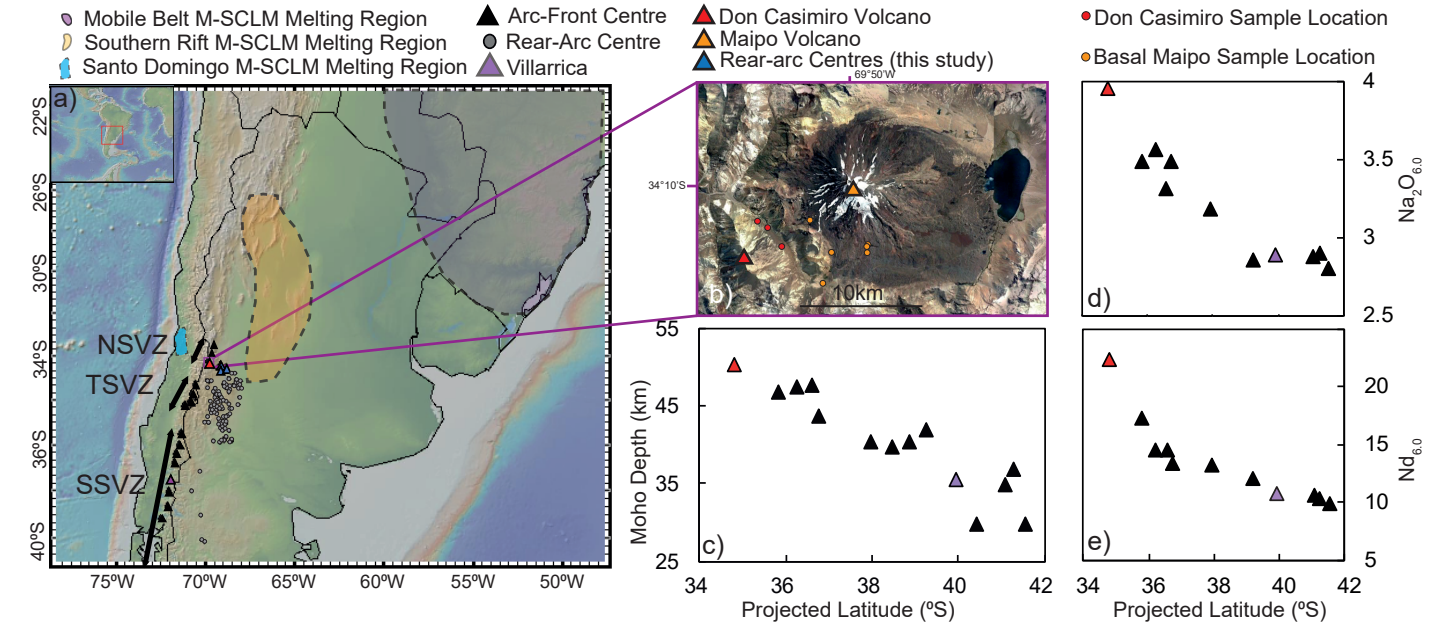
Mobile Belt M-SCLM Melting Region
Southern Rift M-SCLM Melting Region
Santo Domingo M-SCLM Melting Region
Arc-Front Centre
Rear-Arc Centre
Villarrica
Don Casimiro Volcano
Maipo Volcano
Rear-arc Centres (this study)
Don Casimiro Sample Location
Basal Maipo Sample Location
a)
NSVZ
TSVZ
SSVZ
22ºS
26ºS
30ºS
34ºS
36ºS
40ºS
75ºW
70ºW
65ºW
60ºW
55ºW
50ºW
69°50'W
34°10'S
b)
10km
c)
Moho Depth (km)
Projected Latitude (ºS)
d)
$Na_2O_{6.0}$
e)
$Nd_{6.0}$
Projected Latitude (ºS)

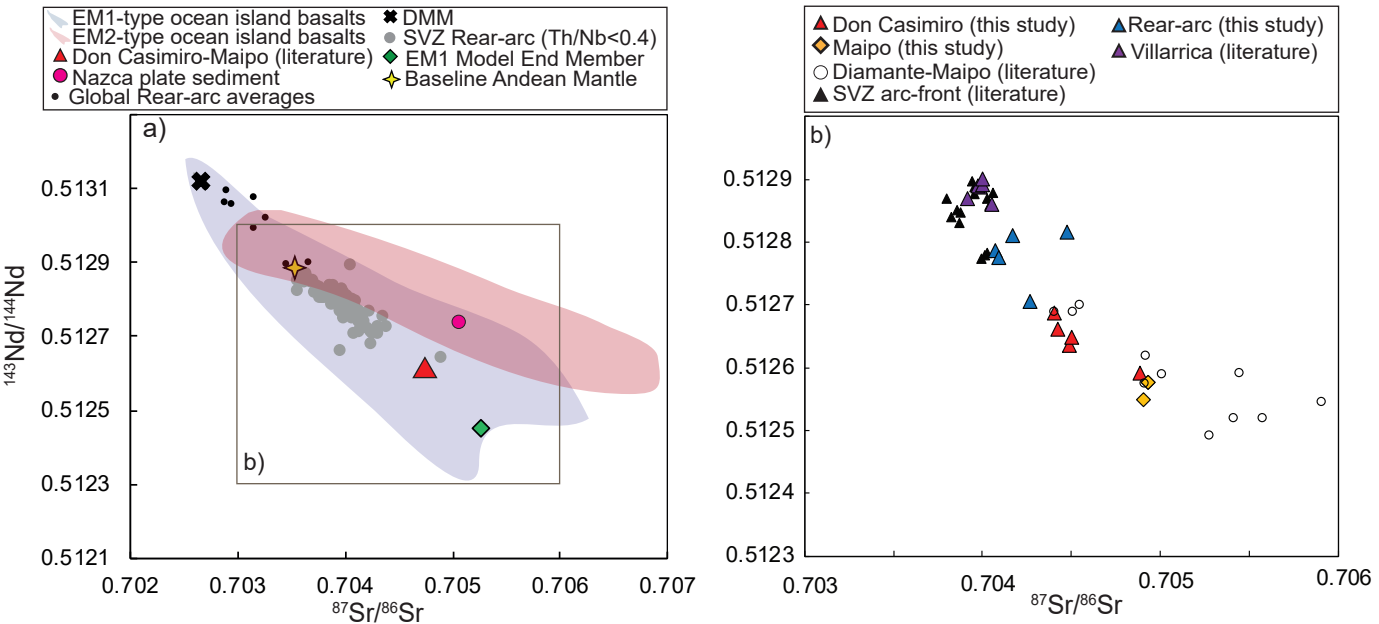
EM1-type ocean island basalts
EM2-type ocean island basalts
Don Casimiro-Maipo (literature)
Nazca plate sediment
Global Rear-arc averages
DMM
SVZ Rear-arc (Th/Nb<0.4)
EM1 Model End Member
Baseline Andean Mantle
a)
b)
143Nd/144Nd
87Sr/86Sr
0.5131
0.5129
0.5127
0.5125
0.5123
0.5121
0.702
0.703
0.704
0.705
0.706
0.707
Don Casimiro (this study)
Maipo (this study)
Diamante-Maipo (literature)
SVZ arc-front (literature)
Rear-arc (this study)
Villarrica (literature)
0.5129
0.5128
0.5127
0.5126
0.5125
0.5124
0.5123
0.703
0.704
0.705
0.706

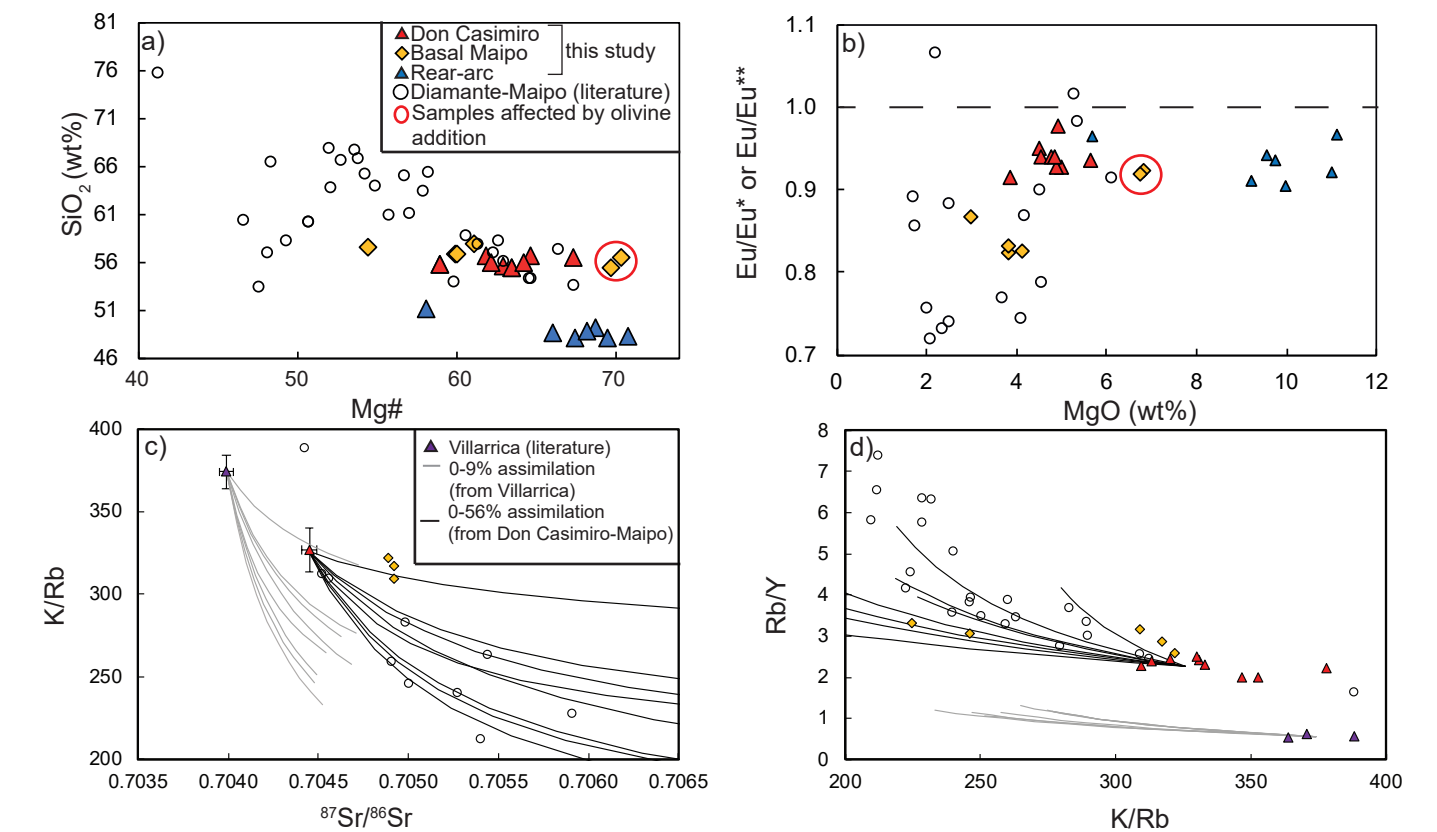
a)
Don Casimiro
Basal Maipo
Rear-arc
this study
Diamante-Maipo (literature)
Samples affected by olivine addition
SiO2 (wt%)
Mg#
b)
Eu/Eu* or Eu/Eu**
MgO (wt%)
c)
Villarrica (literature)
0-9% assimilation (from Villarrica)
0-56% assimilation (from Don Casimiro-Maipo)
K/Rb
87Sr/86Sr
d)
Rb/Y
K/Rb

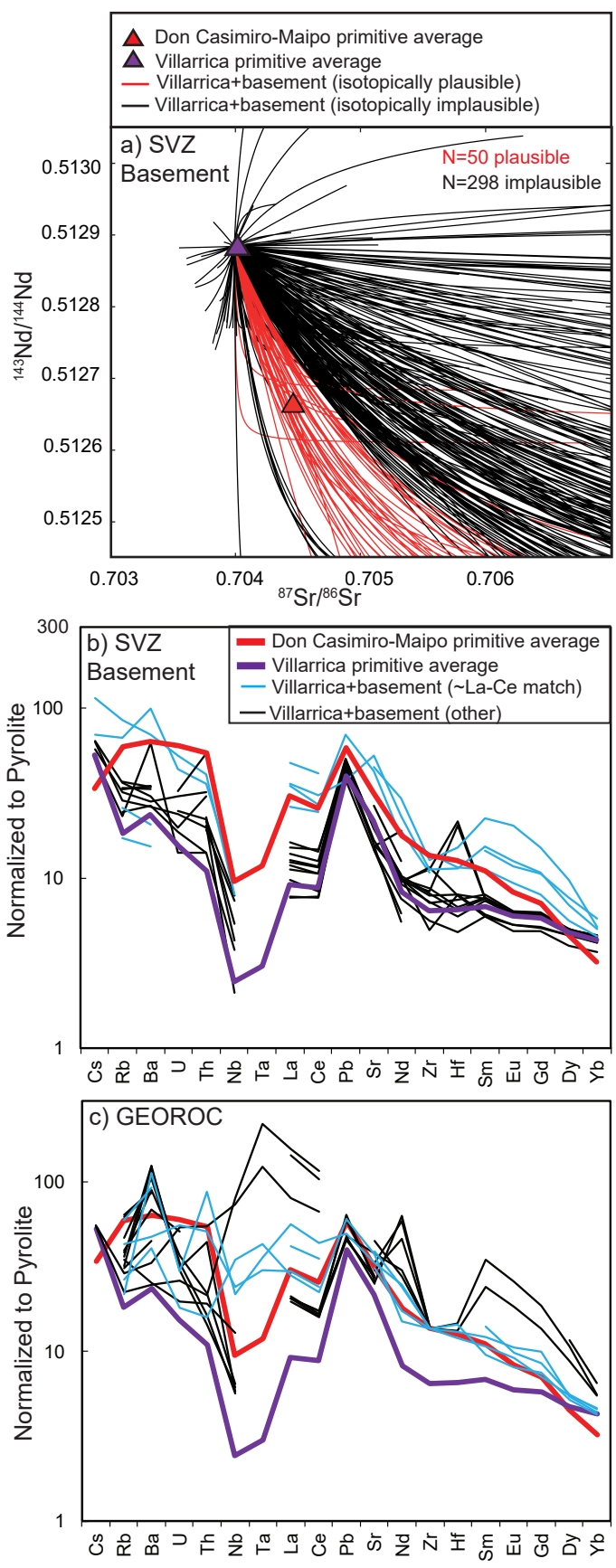
Don Casimiro-Maipo primitive average
Villarrica primitive average
Villarrica+basement (isotopically plausible)
Villarrica+basement (isotopically implausible)
a) SVZ Basement
N=50 plausible
N=298 implausible
143Nd/144Nd
0.5130
0.5129
0.5128
0.5127
0.5126
0.5125
0.703
0.704
0.705
0.706
87Sr/86Sr
b) SVZ Basement
Don Casimiro-Maipo primitive average
Villarrica primitive average
Villarrica+basement (~La-Ce match)
Villarrica+basement (other)
Normalized to Pyrolite
300
100
10
1
Cs Rb Ba U Th Nb Ta La Ce Pb Sr Nd Zr Hf Sm Eu Gd Dy Yb
c) GEOROC
Normalized to Pyrolite
100
10
1
Cs Rb Ba U Th Nb Ta La Ce Pb Sr Nd Zr Hf Sm Eu Gd Dy Yb

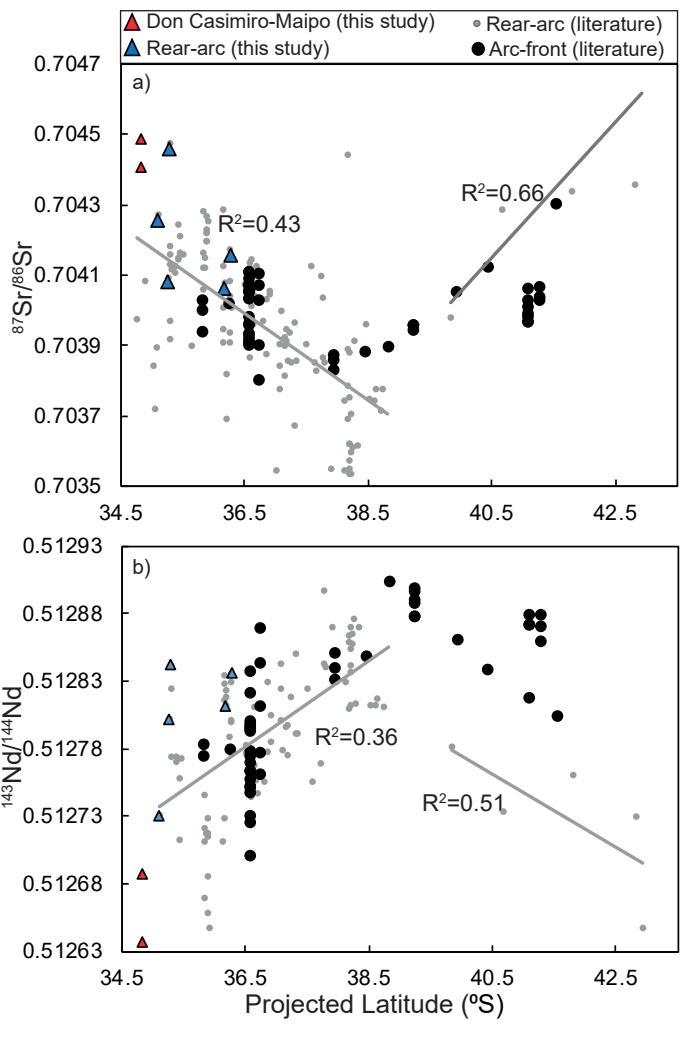
Don Casimiro-Maipo (this study)
Rear-arc (this study)
Rear-arc (literature)
Arc-front (literature)
a)
$^{87}Sr/^{86}Sr$
0.7047
0.7045
0.7043
0.7041
0.7039
0.7037
0.7035
R²=0.43
R²=0.66
b)
$^{143}Nd/^{144}Nd$
0.51293
0.51288
0.51283
0.51278
0.51273
0.51268
0.51263
R²=0.36
R²=0.51
34.5
36.5
38.5
40.5
42.5
Projected Latitude (ºS)

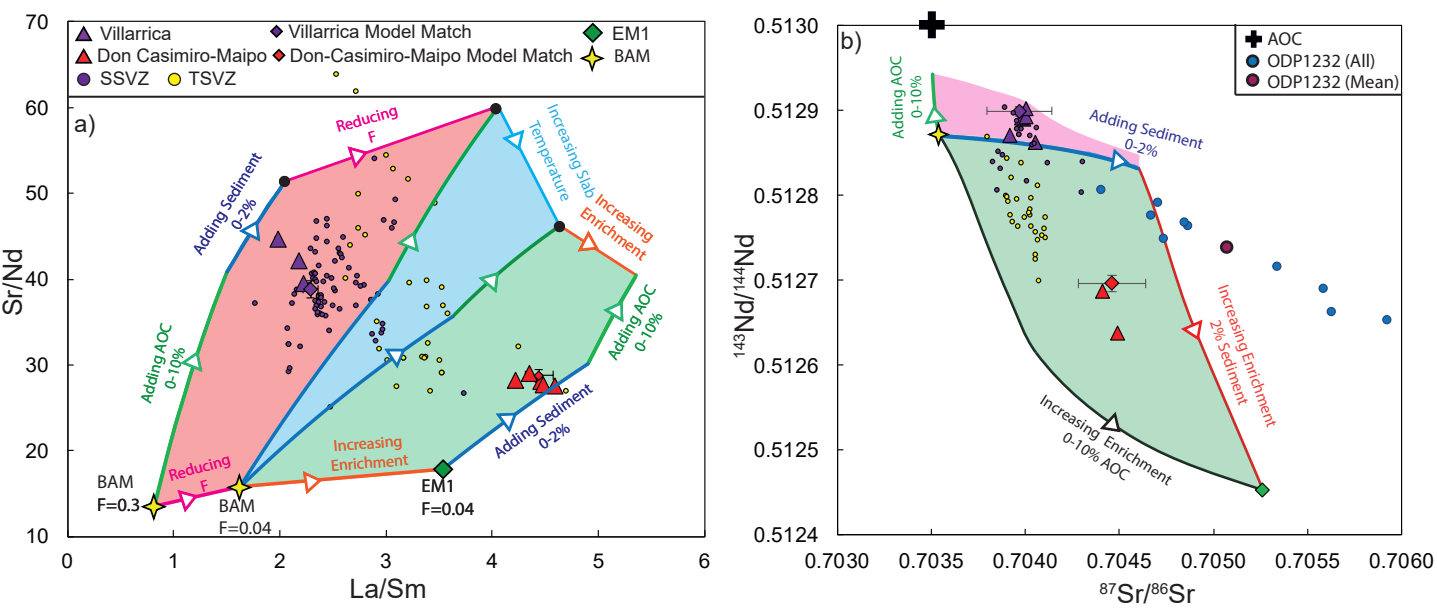
Villarrica
Don Casimiro-Maipo
SSVZ
TSVZ
Villarrica Model Match
Don-Casimiro-Maipo Model Match
EM1
BAM
a)
Sr/Nd
La/Sm
Reducing F
Adding Sediment 0-2%
Increasing Slab Temperature
Increasing Enrichment
Adding AOC 0-10%
Adding AOC 0-10%
Reducing F
Increasing Enrichment
Adding Sediment 0-2%
BAM F=0.3
BAM F=0.04
EM1 F=0.04
b)
AOC
ODP1232 (All)
ODP1232 (Mean)
Adding AOC 0-10%
Adding Sediment 0-2%
Increasing Enrichment 2% Sediment
Increasing Enrichment 0-10% AOC
143Nd/144Nd
87Sr/86Sr

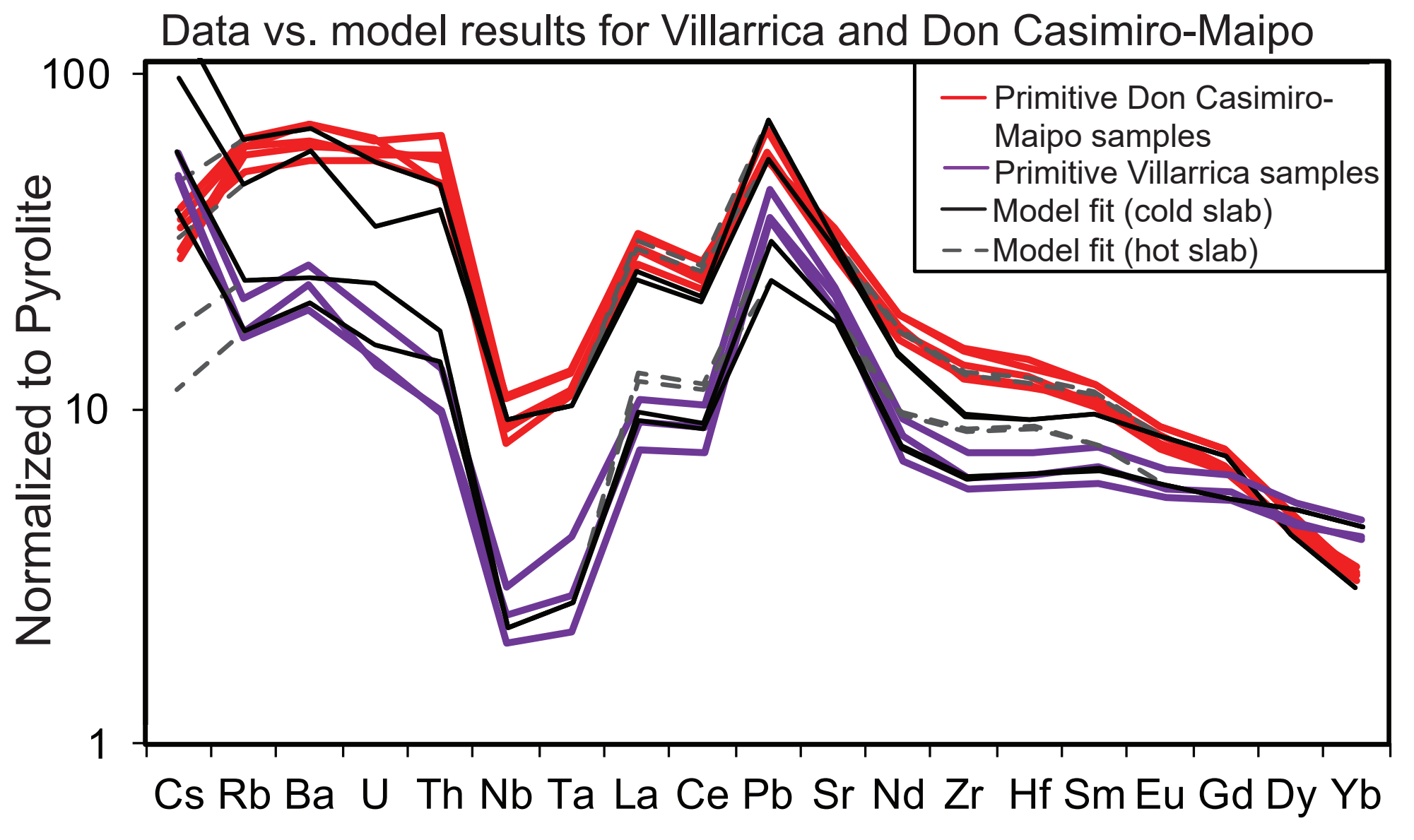
Data vs. model results for Villarrica and Don Casimiro-Maipo
Normalized to Pyrolite
100
10
1
Cs Rb Ba U Th Nb Ta La Ce Pb Sr Nd Zr Hf Sm Eu Gd Dy Yb
Primitive Don Casimiro-Maipo samples
Primitive Villarrica samples
Model fit (cold slab)
Model fit (hot slab)

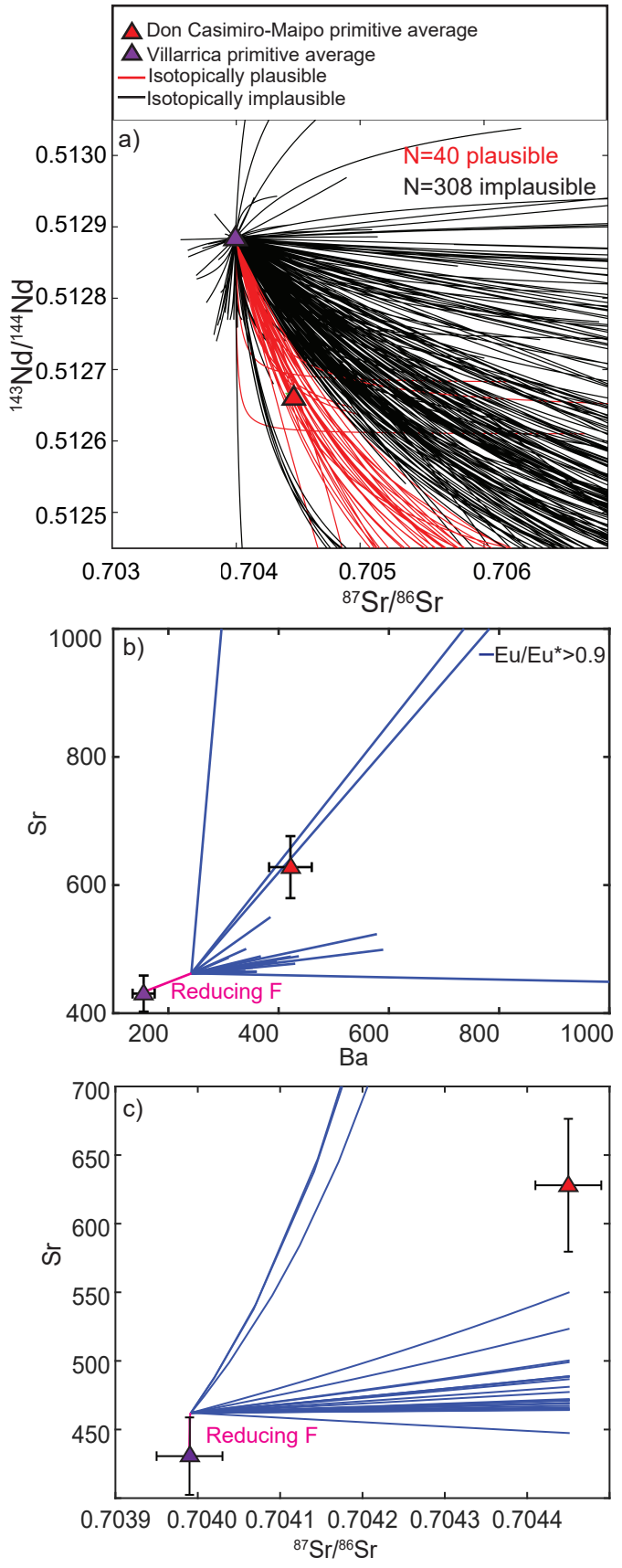
Don Casimiro-Maipo primitive average
Villarrica primitive average
Isotopically plausible
Isotopically implausible
a)
N=40 plausible
N=308 implausible
0.5130
0.5129
0.5128
0.5127
0.5126
0.5125
143Nd/144Nd
0.703
0.704
0.705
0.706
87Sr/86Sr
b)
Eu/Eu*>0.9
1000
800
600
400
Sr
Reducing F
200
400
600
800
1000
Ba
c)
700
650
600
550
500
450
Sr
Reducing F
0.7039
0.7040
0.7041
0.7042
0.7043
0.7044
87Sr/86Sr

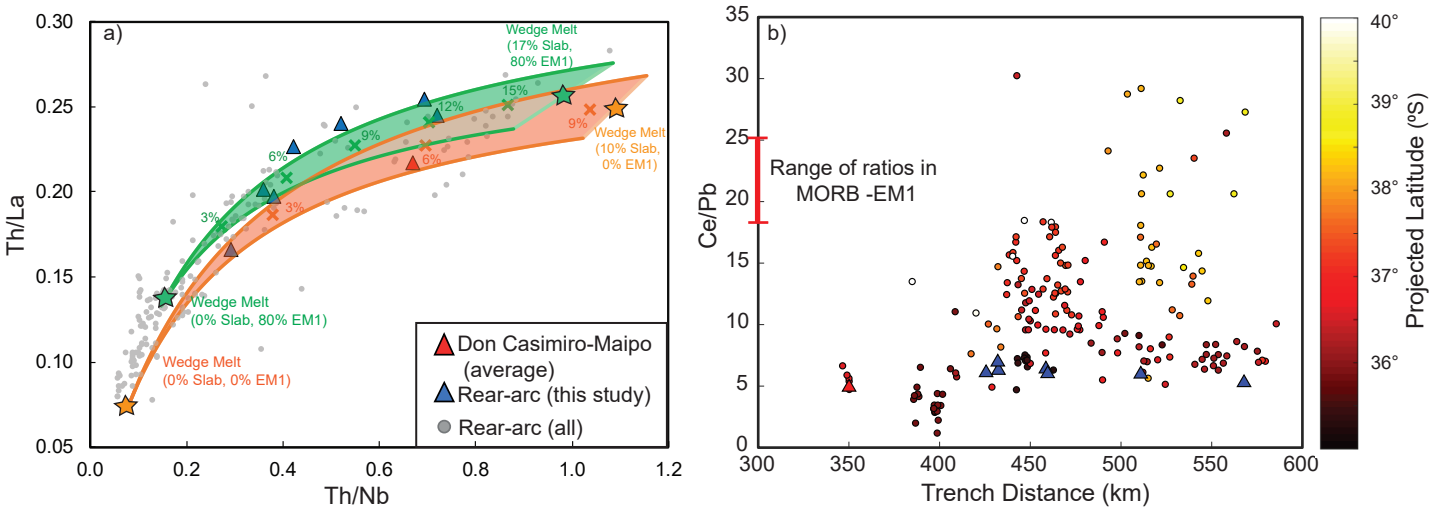
a)
Wedge Melt
(17% Slab,
80% EM1)
Wedge Melt
(10% Slab,
0% EM1)
Wedge Melt
(0% Slab, 80% EM1)
Wedge Melt
(0% Slab, 0% EM1)
3%
6%
9%
12%
15%
Don Casimiro-Maipo
(average)
Rear-arc (this study)
Rear-arc (all)
Th/La
Th/Nb
0.05
0.10
0.15
0.20
0.25
0.30
0.0
0.2
0.4
0.6
0.8
1.0
1.2
b)
Range of ratios in
MORB -EM1
Ce/Pb
Trench Distance (km)
Projected Latitude (°S)
0
5
10
15
20
25
30
35
300
350
400
450
500
550
600
36°
37°
38°
39°
40°

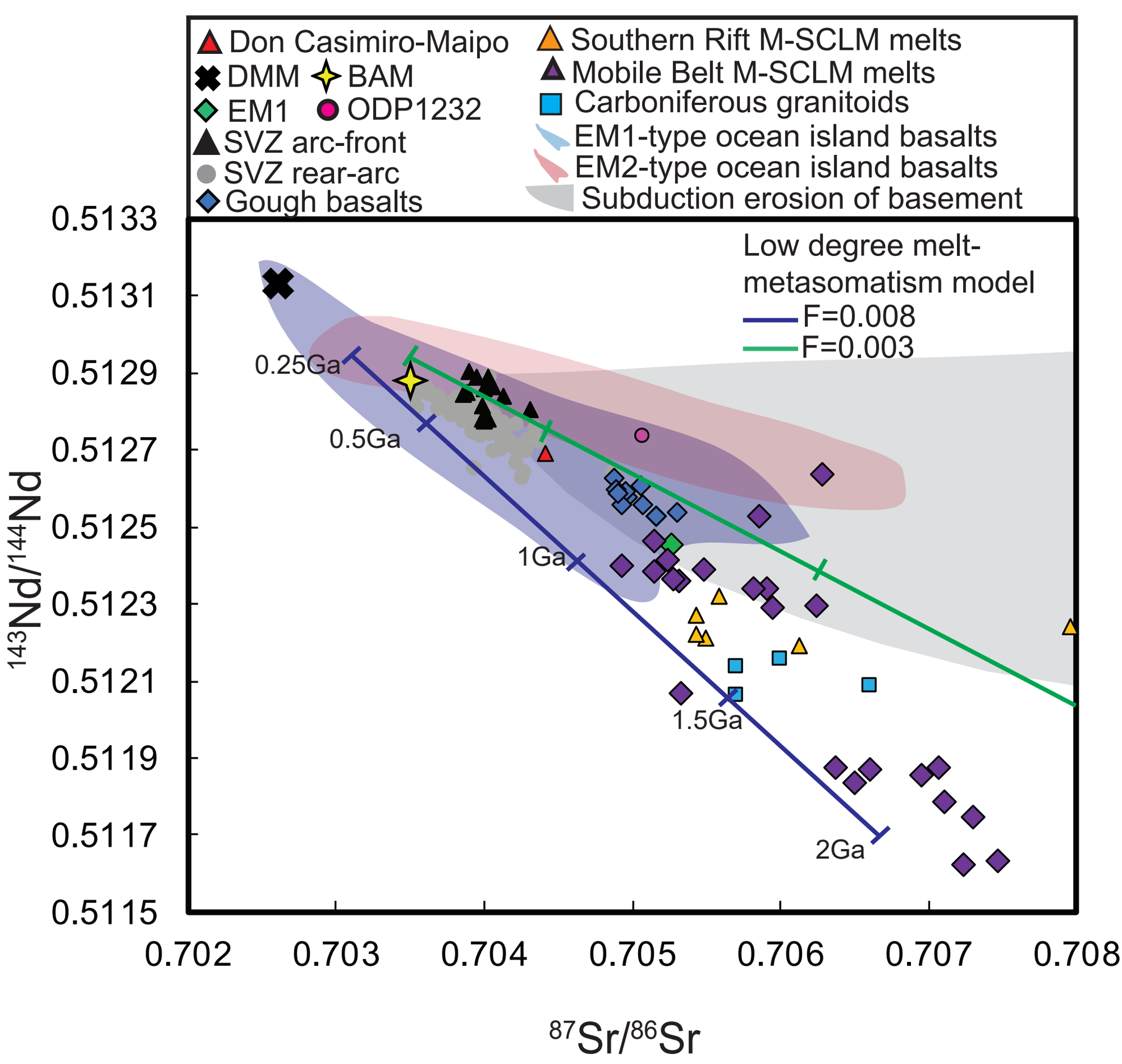
Don Casimiro-Maipo
DMM
BAM
EM1
ODP1232
SVZ arc-front
SVZ rear-arc
Gough basalts
Southern Rift M-SCLM melts
Mobile Belt M-SCLM melts
Carboniferous granitoids
EM1-type ocean island basalts
EM2-type ocean island basalts
Subduction erosion of basement
Low degree melt-metasomatism model
F=0.008
F=0.003
0.25Ga
0.5Ga
1Ga
1.5Ga
2Ga
0.5133
0.5131
0.5129
0.5127
0.5125
0.5123
0.5121
0.5119
0.5117
0.5115
143Nd/144Nd
0.702
0.703
0.704
0.705
0.706
0.707
0.708
87Sr/86Sr

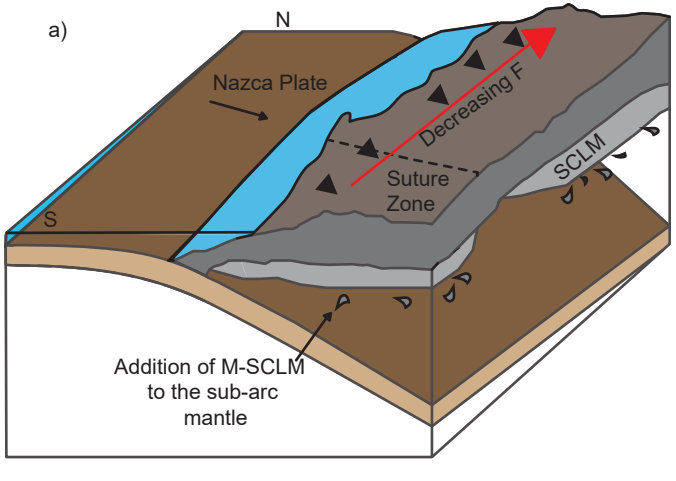
a)
N
Nazca Plate
Decreasing F
Suture
Zone
SCLM
S
Addition of M-SCLM
to the sub-arc
mantle

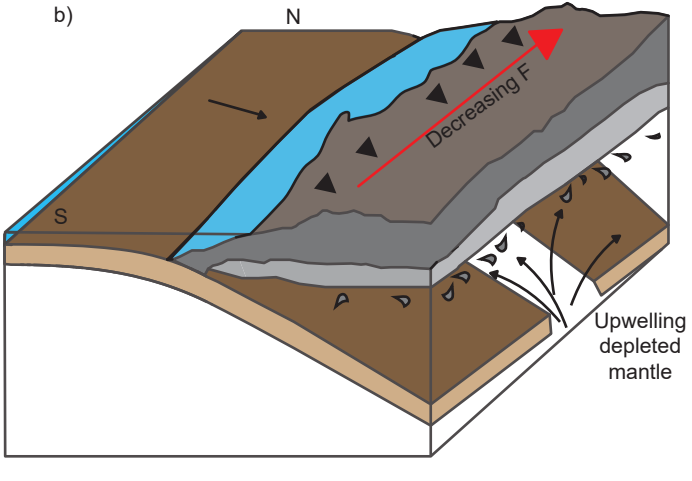
b)
N
Decreasing F
S
Upwelling
depleted
mantle

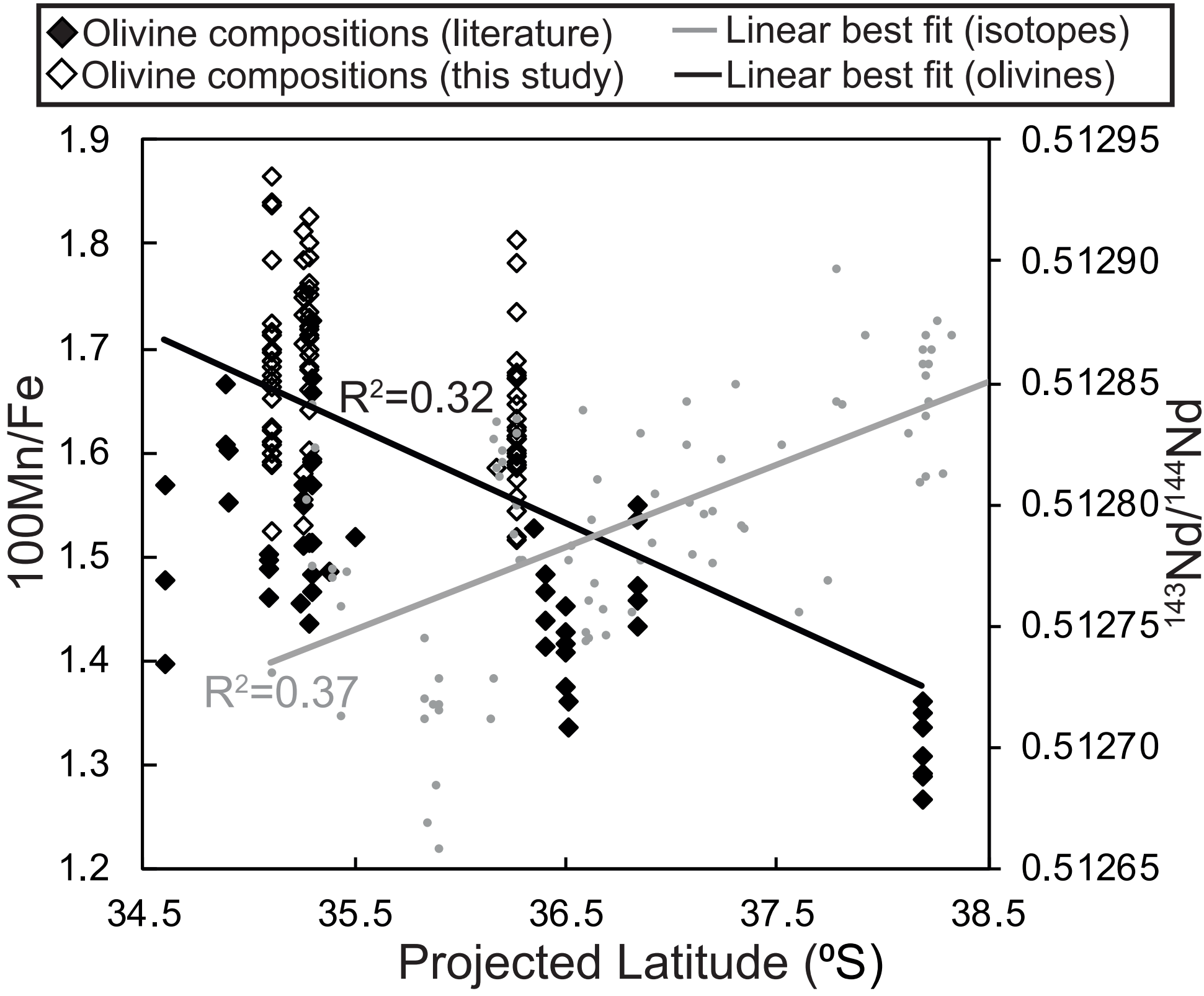
Olivine compositions (literature)
Olivine compositions (this study)
Linear best fit (isotopes)
Linear best fit (olivines)
R²=0.32
R²=0.37
100Mn/Fe
143Nd/144Nd
Projected Latitude (ºS)
1.9
1.8
1.7
1.6
1.5
1.4
1.3
1.2
0.51295
0.51290
0.51285
0.51280
0.51275
0.51270
0.51265
34.5
35.5
36.5
37.5
38.5

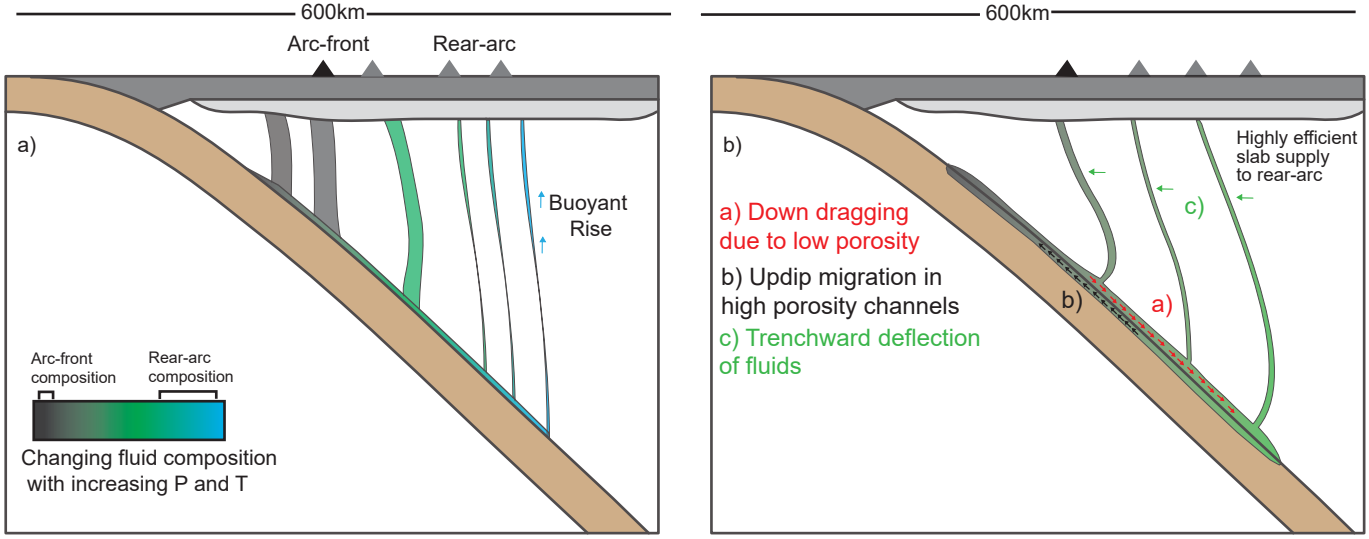
600km
Arc-front
Rear-arc
a)
Buoyant
Rise
Arc-front
composition
Rear-arc
composition
Changing fluid composition
with increasing P and T
600km
b)
Highly efficient
slab supply
to rear-arc
a) Down dragging
due to low porosity
b) Updip migration in
high porosity channels
c) Trenchward deflection
of fluids
c)
b)
a)

Appendix 1: Methods and Sample Details

SIA1 Data and Databases

Whole-rock and olivine analysis from this study is shown in Appendix 3. Compiled rear-arc and Diamante-Maipo literature data used in this study is in Appendix 4. The compilation of SVZ basement compositions is in Appendix 5.

SIA2 Sample Characteristics

Six 100μm sections were made for Don Casimiro-Maipo samples spanning a range of MgO contents. These were scanned using a 5MP slide scanner. Point counting was conducted in JMicroVision by overlaying a 1000 point grid on these scans. Microscope observations were made on any crystals that couldn't be identified with certainty in scans. Crystals smaller than ∼0.05mm were classified as matrix. Amorphous or crystalline material sufficiently distinct from the surrounding matrix that could not be identified as a mineral phase was classified as alteration.

Table SA1: Point counting results for Don Casimiro-Maipo samples (ordered by decreasing wt% MgO).

Sample	MgO (wt%)	Crystals (%)	Matrix (%)	Vesicles (%)	Alteration (%)
G0020315-1	6.82	11	89	0	0.1
G0020315-2	6.73	10	90	0	0.3
G0270215-1D	5.63	17	81	0	0.3
G0270215-1C	4.85	14	85	0	0.2
G0030315-4	3.87	11	72	16	0.0
G0030315-1	2.99	42	48	0	10

Table SA2: Percentage of each phenocryst phase in the crystal fraction. *The fine grained nature of these samples meant that phenocryst phases were harder to identify, so proportions are not as reliable as for other samples.

Sample	Olivine (%)	Clinopyroxene (%)	Plagioclase (%)	Oxide (%)	Orthopyroxene (%)
G0020315-1	66	34	0	0	0
G0020315-2	66	34	0	0	0
G0270215-1D*	6	15	46	33	0
G0270215-1C*	8	20	32	41	0
G0030315-4	7	5	89	0	0
G0030315-1	3	13	82	0	3

Table SA3: Description of Don Casimiro-Maipo samples in thin section.

Sample	Olivine	Plagioclase	Clinopyroxene	Matrix Textures
G0020315-1	Predominantly subhedral-anhedral 2-0.5mm grains, and smaller, <0.5mm anhedral grains. Both types form clots, and show association with clinopyroxene. Most olivines contain oxide inclusions.	No phenocrysts.	Subhedral-anhedral 2-0.5mm grains, often forming clots. Smaller, <0.5mm anhedral grains within the matrix. Some show breakdown in their cores.	Dark, fine grained matrix with white streaks of amorphous material. Needle-shaped matrix plagioclase aligns with these streaks. A few 1-2mm patches of alteration are associated with reacted olivine cores.
G0020315-2	Euhedral 1-3mm grains, subhedral 0.5-2mm clots associated with clinopyroxene, and smaller isolated <1mm anhedral grains.	No phenocrysts.	Subhedral 1-2mm grains, often associated with olivine clots. As above, some show broken down cores.	Dark, fine grained matrix, with white amorphous material in streaks. Small needle-shaped plagioclase shows alignment around large crystals. Abundant anhedral oxide grains.
G0270215-1D	Anhedral <0.2mm grains with abraded edges. These are associated with patches of small red amorphous material.	Blocky to needle-shaped plagioclase. No alignment.	Sub-anhedral, 0.3-1mm grains. These are more commonly associated with the red material than olivines.	Dark, fine grained matrix, with poorly aligned, needle-shaped plagioclase, and dispersed anhedral oxides. Patches of white, amorphous material.
G0270215-1C	Anhedral, <0.1mm grains.	Elongated needles, 20:1 aspect ratio. Aligned in matrix.	Sub-anhedral 0.3-1mm grains, associated with red amorphous material and oxide growth.	Dominated by small, aligned, needle-shaped plagioclase, with euhedral-anhedral opaque oxides.
G0030315-4	Anhedral, <1mm grains, with highly abraded edges, likely these were originally clots.	Large, 2mm+, blocky plagioclase, showing sieve textured cores (indicating rapid growth/cooling/heating).	Euhedral, 2-4mm grains, and smaller, <1mm highly abraded anhedral grains.	Highly vesicular texture. Matrix dominated by glass.
G0030315-1	A few subhedral, 1-2mm olivines. Some associated with large, 1-2mm cubic oxide phases.	Several populations of plagioclase. 1) blocky 2-4mm rectangular macrocrysts, with large fluid inclusions. 2) lath shaped 1-3mm grains, with inclusion-free cores. 3) needle shaped (<1mm) grains, with sieve textured cores.	Euhedral-subhedral, 1-2mm grains with oxide inclusions. Some are also associated with very large, 1-3mm oxide grains. Additionally, one 4mm clot of several grains and oxides is observed. In some places, clinopyroxene forms anhedral intergrowths with plagioclase, and orthopyroxene.	Extremely crystal-rich. Large areas of amorphous material within the slide are associated with large blocky plagioclase macrocrysts. Between phenocrysts, the matrix is dark and amorphous.

SIA3 Methodologies

SIA3.1 Whole Rock Chemistry

Sixteen samples from Don Casimiro-Maipo and seven rear-arc samples were prepared for whole-rock analysis at the University of Oxford. Arc-front lava samples were cleaned in an ultrasonic bath until the water ran clear. These were then split into 2-3cm chunks using a pneumatic rock splitter. Rear-arc samples were wet sieved, and unaltered clasts from the coarsest fraction (>2mm) were hand picked for whole rock analysis. Both sample types were crushed in a steel jaw crusher, and then powdered in an agate ball mill.

Major Element Analysis: Major element analyses was conducted by using a PANalytical Axios Advanced X-ray fluorescence spectrometer at the University of Leicester, UK, following the methods of Knott et al. (2016).

Trace Element Analysis: ∼ 100 mg of each powder as well as reference materials BCR-2a, BHVO-2, W-2a and AGV-2, were digested in ∼4ml of 7.5M HNO_3 and ∼1ml of 24M HF. The samples where then evaporated and redissolved twice in ∼4ml 7.5M HNO_3 to eradicate fluoride precipitates. At this stage, a sample split was made for isotopic analysis. Trace element analyses were conducted using a Perkin Elmer NexION 350D quadrupole ICP-MS for the majority of elements. An additional 1200x dilution and addition of an internal standard containing Rh, Re, and In was achieved using the ESI prepFAST system producing a 6000x solution in which to measure lower concentration elements. All prior dilutions were performed gravimetrically. Sample G0030315-4 was run every four samples, and the entire run was duplicated in reverse order to monitor drift. Drift correction and data reduction were carried out following Turner et al. (2013). Due to malfunctioning of the Prepfast system, a planned run at 60,000x dilution for higher concentration elements using the same method failed. Thus, Sr and Ba concentrations were measured using a Thermo Element 2 ICP-MS (also at the University of Oxford) at a 1,200,000x dilution (performed gravimetrically).

The digestion procedure, and sample homogeneity can be assessed by calculating the % difference between the measured element concentrations of two duplicates produced from the powders of this study, and two from an additional set of samples digested alongside these. Most measurements lie within 5%, suggesting that the digestion process, and samples, were reasonably homogeneous (table SA4).

Isotopic Analysis

Strontium (Sr) and neodymium (Nd) isotope analyses were performed on a Thermo Scientific Triton-series multicollector mass spectrometer at the School of Earth and Environment, University of Leeds. Eleven whole-rock powders were digested alongside those for trace element analysis, followed by subsequent drying and pick up in concentrated ultrapure HNO_3 and HCl acids. The final dried samples were diluted and centrifuged for 15 minutes at 2000 rpm. Sr and Nd were extracted by using Sr-Spec and TRU-spec resins and conventional ion-exchange chromatographic techniques. $^{87}Sr/^{86}Sr$ and $^{143}Nd/^{144}Nd$ ratios were normalized for mass fractionation to $^{86}Sr/^{88}Sr$=0.1194 and $^{146}Nd/^{144}Nd$=0.7219. Samples for Sr were loaded onto previously outgassed W filaments and samples for Nd were loaded onto previously outgassed Re filaments. Sr and Nd were analysed while the current was maintained between 3-5 V (for ^{88}Sr) and 0.4-0.8 V (for ^{144}Nd).

The average $^{87}Sr/^{86}Sr$ obtained from repeated measurements of NIST SRM-987 during the course of this study was 0.710271. Similarly, we measured $^{143}Nd/^{144}Nd$=0.511837 for the LaJolla standard. Two samples (G0020315-2 and G0270215-1C) were analyzed for $^{143}Nd/^{144}Nd$ in a separate run, in which we measured $^{143}Nd/^{144}Nd$=0.511850 for the LaJolla standard. We also successfully reproduced the published USGS standard BHVO-2 values for $^{87}Sr/^{86}Sr$=0.703468 and $^{143}Nd/^{144}Nd$=0.512995 (Weis et al., 2005). Details on the sample preparation and analytical protocols are described in Crummy et al. (2014).

SIA3.2 Correction of Isotopic data of this study and Literature Data

Sr and Nd isotopes from the literature and this study were corrected to be in line with the analytical procedure used for SVZ data presented in Turner et al. (2016). Various standards were corrected to be equivalent to La Jolla=0.511858, NBS 987=0.710235 based on session averages.

Table SA4: % deviation of four duplicates ran during analysis on the "quad" (except starred elements, where % deviation is reported from the "element"). (4) represents a duplicate of G0030315-4, (1) represents a duplicate of MDZ1, 079a and B1 are samples measured in the same run, but for use in a study on the Main Ethiopian Rift. % deviation is defined as (Measurement 1-Measurement 2)/(Average of measurement 1 and 2) x 100.

	% difference (4)	% difference (1)	% difference (079)	% difference (B1)
Li	4.13	1.74	-0.97	0.35
Be	-4.52	60.2	-12.4	1.29
Sc	5.89	-27.0	-20.5	-0.72
V	2.02	-1.95	-0.65	0.15
Cr	3.02	0.41	1.14	-0.99
Ni	3.53	0.74	0.86	1.47
Cu	4.71	-3.94	-0.26	1.76
Rb	3.64	0.28	-9.66	0.30
Sr*	5.54	1.74	0.35	-5.67
Y	2.99	-3.08	-6.18	-0.94
Zr	2.12	-0.29	-0.42	0.32
Nb	3.09	0.21	-0.30	1.16
Cs	8.90	-5.49	-4.43	9.11
Ba*	6.08	3.17	3.65	-2.89
La	3.52	0.58	1.10	0.82
Ce	3.31	-1.09	0.94	0.70
Pr	4.57	0.71	2.05	0.80
Nd	3.29	3.63	-0.88	-0.53
Sm	0.00	2.17	1.35	2.23
Eu	2.21	2.20	1.55	-1.12
Gd	3.09	-2.92	-2.87	1.04
Tb	3.26	-2.17	2.29	0.91
Dy	3.83	-0.60	2.67	0.78
Ho	4.64	-2.73	-0.32	3.88
Er	2.99	4.01	-2.53	3.70
Tm	2.81	-5.67	-3.75	0.51
Yb	2.67	1.49	-0.23	1.69
Lu	1.28	1.41	-3.58	1.15
Hf	3.34	0.93	-0.87	1.40
Ta	-2.98	-0.57	1.60	-0.94
Pb	3.55	-2.14	-9.60	1.72
Th	3.48	-2.05	-17.6	-1.10
U	3.33	-0.09	0.56	-0.11

SIA3.3 Olivine Chemistry

Olivines were picked from the 1000-250μm grain fractions, and mounted in epoxy rings. These mounts were polished and carbon coated for EMPA analysis. Analysis was conducted with an accelerating voltage of 15KeV, a current of 100nA and a 10μm spot size. St John's Island and Fayalite were run as secondary standards, with % recoveries reported in table SA5.

LA-ICP-MS analysis was conducted at the University of Cambridge. Three instrument runs were performed over two days. The run conditions were 20Hz, 80µm, 9.5J/cm^2, 0.8L/min of gas flow for He and Ar. Where possible, three spots were placed in the centre of the olivine, with no overlap. For very small grains, only 2 spots were placed, as it is preferable to have fewer spots nearer the centre than more spots towards the grain edges, due to the reasonably high diffusivity of elements of interest to this study. To allow drift correction, 3 spots on each of

NISTSRM612, NISTSRM610, 06SGOL03 (inhouse olivine standard) and BD4074OL-7 (a San Carlos olivine) were run every 30 analyses. ^{29}Si was used as an internal standard, with values obtained from EMPA grain averages. Signals were selected using Glitter Processing software, with normalization to NISTSRM612 via a quadratic drift correction. This was effective at removing drift, as determined by observing the stability of NISTSRM610, 06SGOL03 and BD4074OL-7 following this correction. Multiple secondary standards were run to assess the accuracy of the measurement for elements of interest (NISTSRM610, NISTSRM614, BCR-2G). Measurement of inhouse olivines O6SGOl03 and BD407OL-7 provided an excellent assessment of the success of the drift correction performed on glass standards. Elements of interest in this study drifted by less than 7%. Although Mn and Ni recovery on glass standards were good, these elements were recovered more poorly on BCR-2G. This, and the fact that previous studies in this area have used EMPA Ni and Mn data, resulted in us choosing to use EMPA data for consistency, as most of the peridotite-pyroxenite ratios involve normalization to Fe (which is reported from EMPA). Detection limits, and 1 sigma uncertainties calculated from Glitter for a representative sample (MDZ2) are shown in table SA6.

Table SA5: Peak count times, and calibration materials used. % recovery calculated below is defined as Measured Average/Published Average x 100. Where no published value exists for a standard, - is shown. Detection limits are reported from 9 spots on MDZ8. These are assumed to be representative of the analysis as a whole.

	Mn	Fe	Mg	Si	Ca	Ni
Peak count times (s)	20	30	20	20	70	70
Calibration material	Mn metal	Andradite	MgO	Albite	Wollastonite	Ni metal
% Rec Fayalite	97.7	94.2	-	99.6	97.0	-
% Rec St Johns Island Olivine	106.1	96.1	99.6	99.2	-	90.1
Detection limit (ppm)	173	197	173	98	74	137

Table SA6: Minimum (99% Confidence) detection limits (ppm), and 1 sigma uncertainties (ppm) for all spots on MDZ2, taken as representative for the analysis as a whole. The mass in brackets represents the isotope measured on the ICP-MS.

Element	MDL	1 σ uncertainty
Li(7)	0.115	0.151
Na(23)	1.121	6.92
Al(27)	0.318	39.3
P(31)	13.76	47.3
Ca(43)	133	192
Sc(45)	0.062	0.412
Ti(47)	0.551	18.4
V(51)	0.043	0.504
Cr(53)	0.578	56.0
Mn(55)	0.136	88.4
Co(59)	0.049	7.91
Ni(60)	0.171	191
Cu(65)	0.351	0.416
Zn(66)	0.373	10.1
Ga(69)	0.042	0.049
Ge(72)	0.370	0.208
Y(89)	0.037	0.025
Zr(90)	0.033	0.052
Nb(93)	0.035	0.021

Table SA7: % recovery of NISTSRM610 (average of 3 spots). (x,y) refers to when this secondary standard was run, x referring to the instrument run (1-3), and y to the order of measurement within a given run. These values were used to check the success of the quadratic drift correction. Across the three instrument runs, most elements drift by less than 10%.

Element	(1,1)	(1,2)	(1,3)	(1,4)	(1,5)	(2,1)	(2,2)	(2,3)	(2,4)	(3,1)	(3,2)	(3,3)	(3,4)	AVERAGE
Li(7)	98.0	105.5	103.7	106.7	105.9	107.3	104.3	101.1	103.6	108.0	99.6	96.8	98.2	103.0
Na(23)	98.2	105.7	107.0	106.1	105.9	105.9	104.9	101.4	103.9	105.0	103.0	101.1	102.1	103.9
Al(27)	102.3	105.5	105.9	106.2	107.8	108.3	104.2	104.9	107.3	105.6	107.2	103.5	104.9	105.7
P(31)	107.8	105.2	99.7	130.9	194.5	100.5	103.9	101.0	100.5	125.0	113.1	117.6	133.9	118.0
Ca(43)	95.9	103.7	100.6	106.7	107.3	105.2	102.5	99.2	102.2	105.2	100.1	99.5	104.5	102.5
Sc(45)	98.7	109.1	108.0	109.8	108.8	110.2	110.9	105.6	108.9	108.5	106.7	108.0	109.6	107.9
Ti(47)	115.2	120.8	116.9	120.0	119.0	125.1	128.7	124.5	125.5	125.3	125.9	122.8	125.4	122.7
V(51)	95.7	101.9	100.1	105.2	105.8	104.8	102.6	100.1	105.1	105.9	101.7	99.9	103.7	102.5
Cr(53)	103.4	107.7	109.4	113.6	119.5	120.7	115.9	112.1	115.1	114.1	111.4	112.7	116.7	113.2
Mn(55)	94.6	100.0	100.0	103.7	102.4	105.1	100.2	99.0	103.5	104.9	97.1	96.1	97.7	100.3
Co(59)	95.5	103.0	101.7	103.7	100.8	104.2	102.0	98.9	104.3	103.6	101.0	100.3	103.4	101.7
Ni(60)	92.1	100.9	99.8	103.7	99.9	105.6	100.1	98.2	100.0	104.3	101.8	100.5	102.2	100.7
Cu(65)	89.9	98.8	97.3	100.1	97.5	100.5	98.4	94.9	99.0	100.1	96.0	95.9	97.6	97.4
Zn(66)	98.5	104.1	102.3	108.8	110.2	111.1	104.4	100.1	106.6	109.9	106.4	104.1	102.9	105.3
Ga(69)	92.2	97.7	96.5	101.1	101.5	101.7	99.0	97.2	99.4	101.4	98.9	98.3	100.8	98.9
Ge(72)	81.5	86.7	85.7	89.1	88.8	92.4	89.0	85.6	86.6	92.0	87.5	87.8	89.8	87.9
Y(89)	93.1	102.1	99.8	102.8	102.1	104.0	102.9	100.5	100.3	102.5	101.4	101.8	103.8	101.3
Zr(90)	89.8	95.9	94.6	97.9	98.1	98.6	98.5	94.6	95.4	97.5	96.8	96.0	98.7	96.3
Nb(93)	92.8	99.9	98.9	102.4	101.7	102.2	102.2	98.1	100.2	102.9	99.9	99.2	101.1	100.1

Table SA8: % recovery of BCR-2G, using averages from 3 spots, and % recovery of NISTSRM614. The % recovery for NISTSRM614 is not shown for the first run. These were the first spots ran by the laser, and it has been shown that the system takes a few spots to warm up and settle after switching from solution mode to laser mode.

Element	(1,1)	(2,1)	(2,2)	(3,1)	(3,2)	BCR-2G Average	(2,1)	(3,1)	NISTSRM614 Average
Li(7)	100.2	104.5	101.7	105.8	94.6	101.4	84.4	103.7	94.1
Na(23)	96.2	99.1	97.0	101.4	96.9	98.1	105.5	103.1	104.3
Al(27)	103.8	103.4	99.9	104.6	103.3	103.0	106.6	106.3	106.4
P(31)	101.3	84.9	86.8	108.4	120.1	100.3	268.2	260.0	264.1
Ca(43)	99.0	97.9	98.9	101.1	99.1	99.2	106.2	103.7	105.0
Sc(45)	97.5	102.1	96.4	100.8	99.9	99.3	217.1	185.9	201.5
Ti(47)	107.3	108.4	105.2	110.9	106.3	107.6	122.1	101.3	111.7
V(51)	97.6	100.1	101.1	102.8	99.6	100.2	109.7	99.9	104.8
Cr(53)	93.2	104.4	92.9	97.1	101.1	97.7	94.8	113.0	103.9
Mn(55)	92.4	96.6	94.9	98.5	90.0	94.5	105.6	89.7	97.7
Co(59)	99.0	97.8	97.0	97.9	96.2	97.6	92.6	95.0	93.8
Ni(60)	89.4	86.9	83.8	90.2	86.5	87.4	107.9	71.8	89.8
Cu(65)	71.0	72.5	67.5	71.1	69.6	70.3	88.8	109.0	98.9
Zn(66)	121.5	134.0	127.4	134.9	120.7	127.7	91.4	89.2	90.3
Ga(69)	111.6	117.1	109.2	118.4	114.5	114.2	96.9	93.9	95.4
Ge(72)	99.6	112.9	95.6	101.1	102.4	102.3	86.3	110.8	98.5
Y(89)	87.3	90.0	81.9	90.6	89.1	87.8	102.0	99.4	100.7
Zr(90)	84.5	87.0	78.3	87.7	86.3	84.7	90.3	91.6	90.9
Nb(93)	88.6	91.6	86.6	91.0	90.2	89.6	93.7	99.3	96.5

SIA4 Mantle Melting Model Details

As discussed in the text, this study uses an updated version of the model of Turner and Langmuir (2015b). Below, the justification of various inputs to the model are discussed. The updated Matlab scripts ADD_SLAB.m, ADD_SLAB_HOTP.m and ModeMelt_Hydrous.m have been uploaded into the supplementary information.

SIA4.1 Model Partition Coefficients

Hydrous Partition Coefficients for Mantle Melting: This study utilizes hydrous partition coefficients and mantle modes from Turner and Langmuir (2015b; detail in their supplement). However, we slightly updated the partitioning behaviour of several elements:

1) The bulk partition coefficient of Eu is obtained by a log extrapolation from those of Sm and Gd:

$$\mathrm{Kd}_{Eu} = (\mathrm{Kd}_{Sm} * \mathrm{Kd}_{Gd})^{0.5}$$

correcting an error in Turner and Langmuir (2015b).

2) The partition coefficient of Hf is assumed to be equal to that of Sm.

3) The partition coefficient of Zr is approximated as:

$$\mathrm{Kd}_{Zr} = (\mathrm{Kd}_{Nd} * \mathrm{Kd}_{Sm})^{0.5}$$

Hydrous Partition Coefficients for slab melting: As above, this study uses slightly adapted partition coefficients for slab melting to those in Turner and Langmuir (2015b). These lie within the limits of experimental values (figure SA1). The partition coefficients for the LREE (La, Ce, Nd, and Sm) were reduced by 40% to reflect the hotter slab underneath Don Casimiro-Maipo (inline with experimental high temperature partitioning results; figure SA1). Additionally, the partition coefficients of Zr and Hf were reduced, and 70% of Cs was assumed to be lost to the forearc.

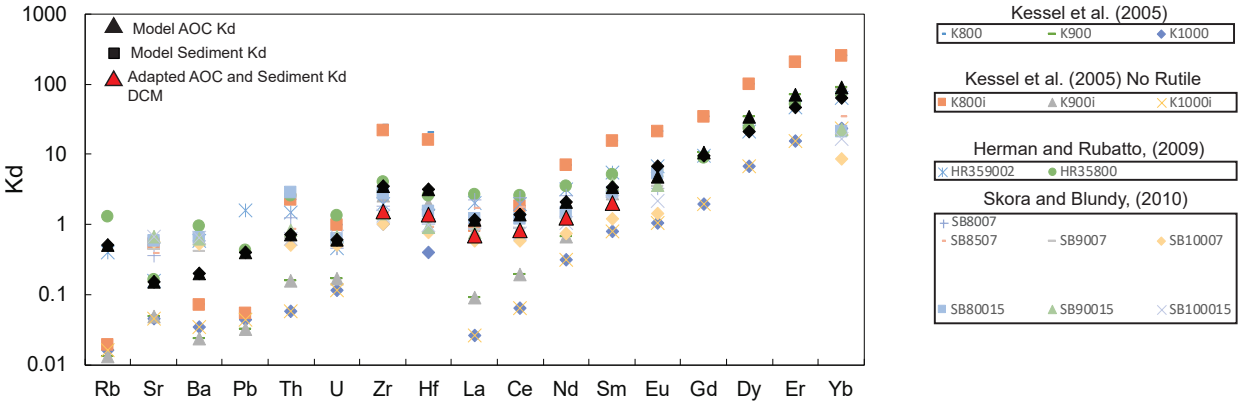

Figure SA1: Slab melting partition coefficients lie within experimental values for 800-1000°C.

SIA4.2 Model End-Members

"Ambient Andean Mantle" (Depleted Mantle End-Member): The isotopic composition of the depleted mantle end member was set to $^{87}Sr/^{86}Sr$=0.70355 and $^{143}Nd/^{144}Nd$=0.512871, the isotopic composition of sample 126171 of Soager et al. (2013) following the isotopic correction discussed above. This sample lies at the depleted end of the rear-arc array, and thus reflects the composition of the Andean mantle prior to the addition of EM1 enrichment. For trace element modelling, the depleted mantle end-member is DMM of Workman and Hart (2005).

AOC: The subducting Nazca plate has Pacific affinities. Trace element concentrations were obtained from melting of N-MORB (Gale et al., 2013) at 876°C, F=0.3. The isotopic composition of AOC was set to $^{87}Sr/^{86}Sr = 0.7035$, $^{143}Nd/^{144}Nd = 0.5130$.

Sediment: The trace element composition of the sediment end-member was obtained from 33 samples of ODP1232 (c.f. Turner et al., 2017). To produce an envelope of model results for trace elements and isotopes, one standard deviation of measured samples were added and subtracted to the mean. Three outliers were discarded based on their anomalously high Sr isotope ratios.

Enriched EM1 end-member: Enrichment at Gough represents a mix of M-SCLM, and ambient mantle. The isotopic signature of recycled M-SCLM depends on the storage time (Turner et al., 2017). As several samples within this study have signatures more enriched than Gough, we use the isotopic composition of a sample from Pitcairn (57DS9; Stracke et al., 2003) as the EM1-like isotopic end member. This lies at the enriched end of the field

enclosing EM1-type ocean island basalts. The trace element concentration was obtained from the inversion of Turner et al. (2017), with a few changes:
1) the bulk Eu partition coefficient was set at:

$$\mathrm{Kd}_{Eu} = (\mathrm{Kd}_{Sm} * \mathrm{Kd}_{Gd})^{0.5}$$

correcting an error in Turner et al. (2017) where it was set at 0.
2) The Zr concentration in Gough primary melts was adjusted to the standard EM1 value Zr/Hf = 45.
3) Zr partition coefficients were extrapolated from Salters and Longhi (1999).
4) Nb and Ta partition coefficients were taken as $\mathrm{Kd}_{La}/3$, based on ratios from Workman and Hart (2005).

Table SA9: Gough mantle source composition used in this study compared to that of Turner et al. (2017; T2017).

	Eu	Zr	Nb	Ta
This study	0.130	6.70	0.403	0.024
T2017	0.0234	11.47	0.472	0.028

SIA5 References

Crummy, J., Savov, I.P, Navarro-Ochoa, C., Morgan, D., Wilson, M., 2014. High-K mafic Plinian eruptions of Volcán de Colima, México, Journal of Petrology, 55 (10). pp.1-18.

Kessel, R., Schmidt, M.W., Ulmer, P. and Pettke, T., 2005. Trace element signature of subduction-zone fluids, melts and supercritical liquids at 120–180 km depth. Nature, 437(7059), pp.724-727.

Knott, T.R., Branney, M.J., Reichow, M.K., Finn, D.R., Coe, R.S., Storey, M., Barfod, D. and McCurry, M., 2016. Mid-Miocene record of large-scale Snake River–type explosive volcanism and associated subsidence on the Yellowstone hotspot track: The Cassia Formation of Idaho, USA. Bulletin, 128(7-8), pp.1121-1146.

Roduit, N. JMicroVision: Image analysis toolbox for measuring and quantifying components of high-definition images. http://www.jmicrovision.com (accessed 4th January 2017).

Salters, V. and Longhi, J. (1999). Trace element partitioning during the initial stages of melting beneath mid-ocean ridges. Earth and Planetary Science Letters 166: 15-30. doi: 10.1016/S0012-821X(98)00271-4.

Turner, S.J., Izbekov, P. and Langmuir, C., 2013. The magma plumbing system of Bezymianny Volcano: Insights from a 54 year time series of trace element whole-rock geochemistry and amphibole compositions. Journal of Volcanology and Geothermal Research, 263, pp.108-121.

Weis, D., Kieffer, B., Maerschalk, C., Pretorius, W., Barling, J. 2005. High-precision Pb-Sr-Nd-Hf isotopic characterization of USGS BHVO-1 and BHVO-2 reference materials. Geochemistry Geophysics Geosystems, 6, Q02002.

Appendix 2

SIB1 Evidence for Olivine Addition

EMPA analysis indicates that Don Casimiro-Maipo olivines lie significantly below the olivine-whole rock equilibrium line (Figure SB1a), indicating excess olivine accumulation. The two most primitive samples, which are from the basal section of Maipo volcano, can be related to the otherwise coherent liquid line of descent among the Diamante Caldera samples by the addition of 7 wt. % Fo 81 olivine (figure SB1b-d.). All samples have phenocrysts of olivine and clinopyroxene, so this trend is not consistent with fractionation of these two phases together. Olivine may have been accumulated from a mush pile produced by fractionation before clinopyroxene appears on the liquidus. This serves as an excellent example of the importance of utilizing individual mineral analyses in conjunction with whole-rock data when interpreting subtle geochemical variations within individual volcanic groups. While it is tempting to represent the parental composition of a volcanic group using the most olivine-phyric samples (6-7vol% olivine, in this case), such samples can often have more complicated petrogenetic histories.

SIB2 Changes in Slab Conditions Inferred from Zr-Hf Anomalies

Using Hf/Sm as a proxy, we find that rear-arc and most arc-front volcanics have a similar range of Zr-Hf values, but Don Casimiro-Maipo has a less pronounced Zr-Hf anomaly (figure SB2). The smaller Hf/Sm (and thus Zr-Hf anomaly) at Don Casimiro-Maipo may reflect the fact that the slab is slightly hotter, which causes residual slab zircon to become more soluble in the slab melt (Hirai et al., 2018).

SIB3 Evidence for AFC processing

As mentioned briefly in the main text, when samples from the entire Diamante-Maipo caldera complex are considered, the correlations between $^{87}Sr/^{86}Sr$ and $^{143}Nd/^{144}Nd$ and indices for fractionation and assimilation (MgO and Eu/Eu*) provide strong evidence for AFC (figure SB3)

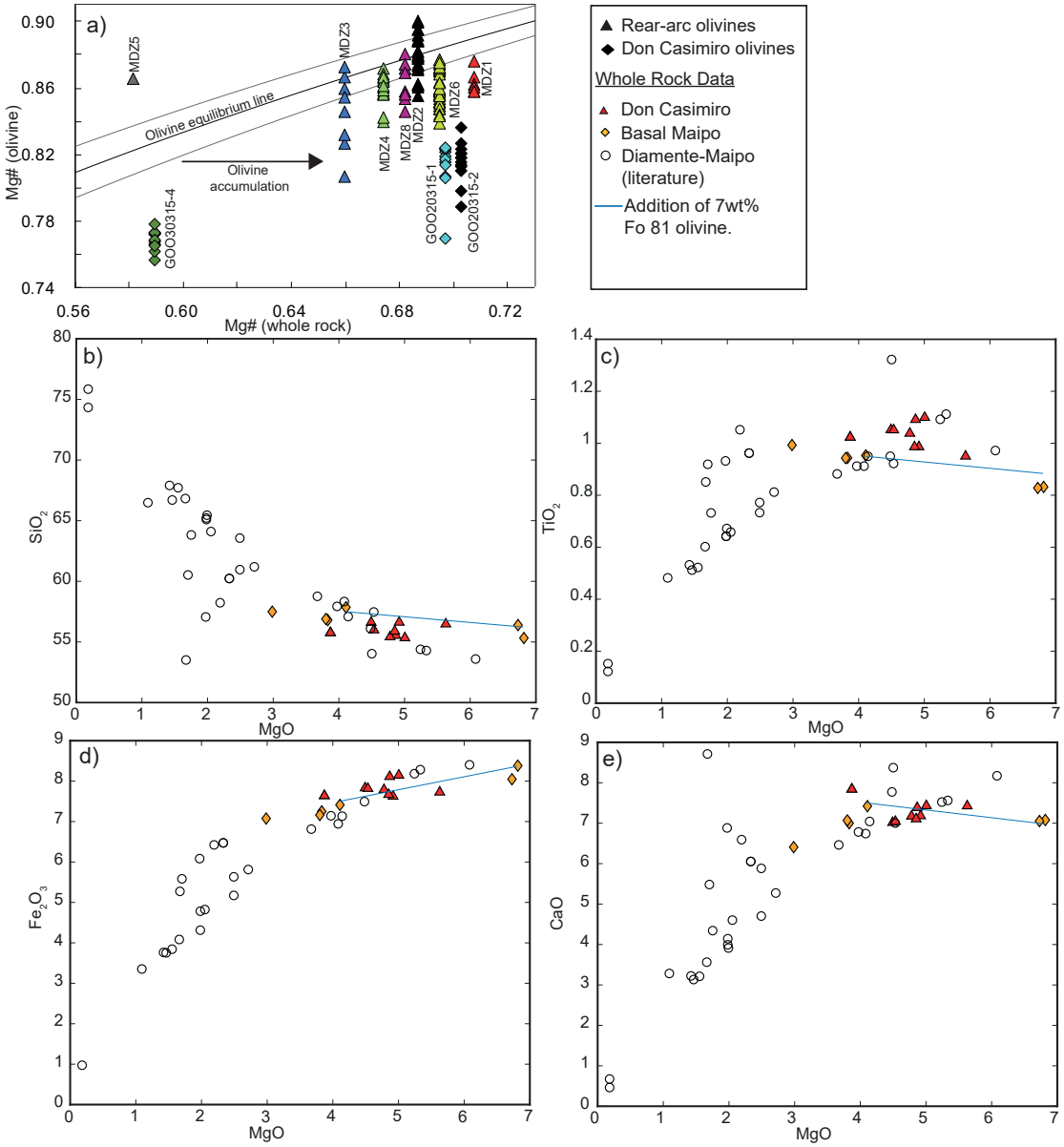

Figure SB1: a) Don Casimiro-Maipo samples show strong evidence for olivine addition, with olivine compositions plotting below an equilibrium line calculated using Roeder and Emslie (1970), Kd=0.3±0.03, assuming whole-rock Fe^{3+}/Fe_T=0.3 (Holm et al., 2016). Most rear-arc olivines plot near to or below the equilibrium line, suggesting minor olivine addition (assuming whole-rock Fe^{3+}/Fe_T=0.15, Søager et al., 2015b). b-d) Addition of 7 wt% Fo 81 olivine from more evolved Maipo samples produces a good match to the most primitive samples, showing that their high MgO contents are spurious. Diamante-Maipo whole-rock data literature data used in this study is from Hickey et al. (1986), Futa and Stern, (1988), Sruoga et al. (2005), Holm et al. (2014) and Hickey et al. (2016).

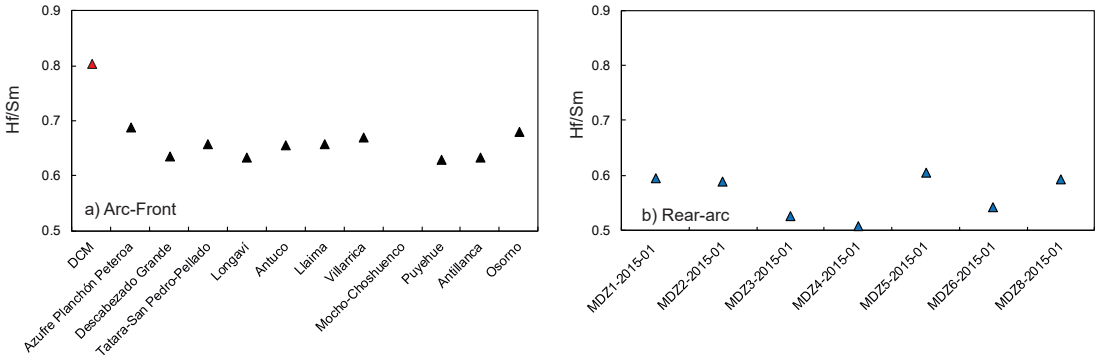

Figure SB2: a) Don Casimiro-Maipo has a significantly different Hf/Sm signature to the rest of the SVZ (data for other centers from Turner et al., 2016). b) Rear-arc centers of this study have similar Hf/Sm ratios to the SVZ arc-front as a whole.

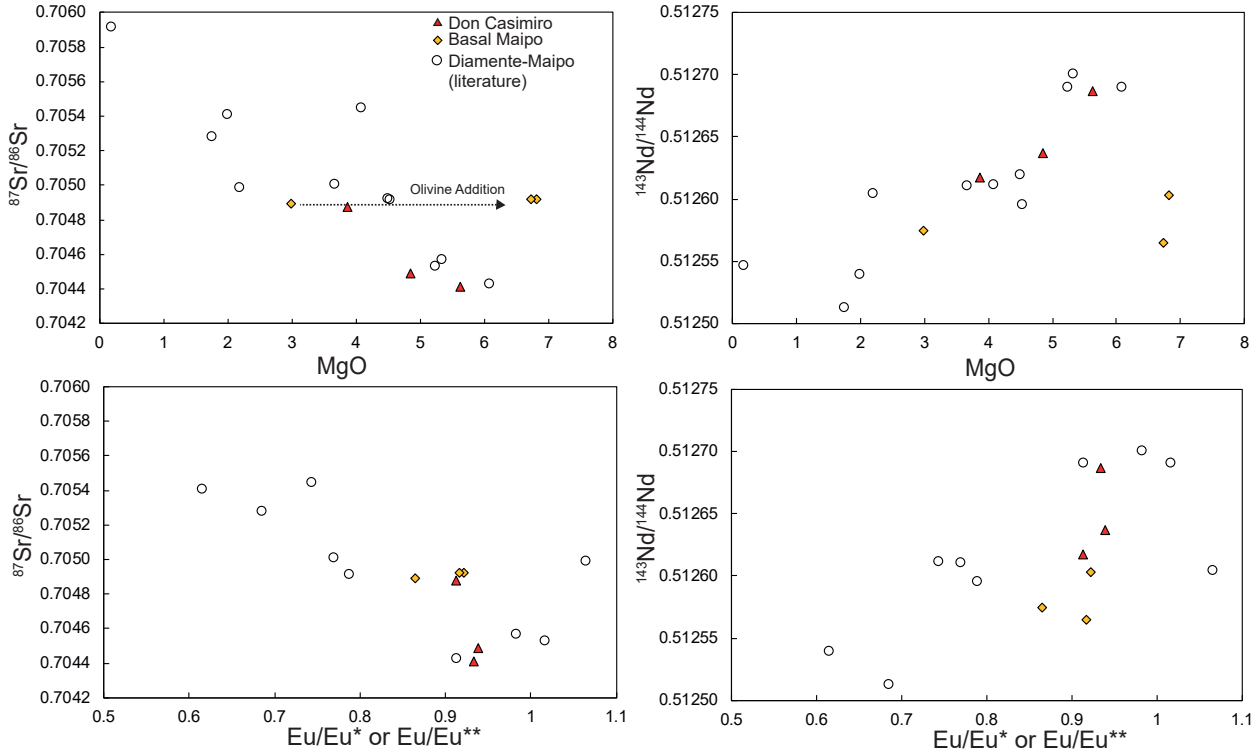

Figure SB3: Within the Diamante-Maipo Caldera, isotopic enrichment increases with assimilation and fractionation. The signal of olivine addition for the two most primitive Maipo samples is also clear.

SIB4 Olivine Chemistry

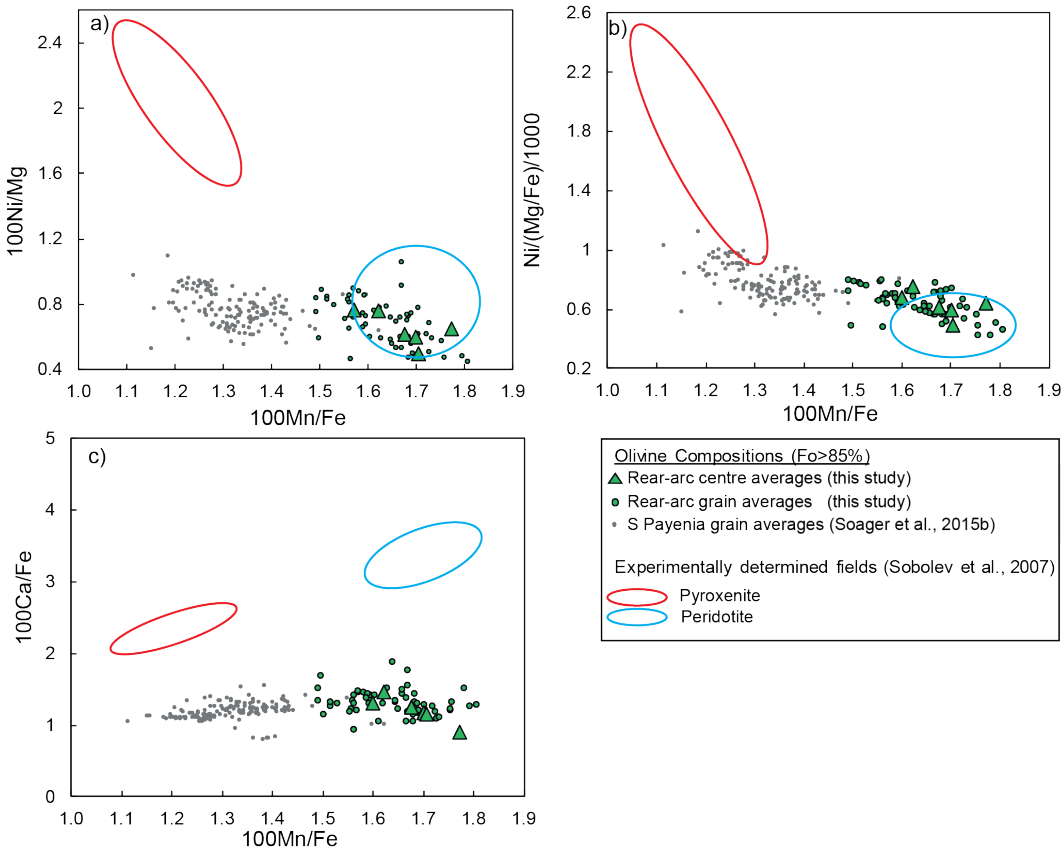

Figure SB4: Olivine analysis of this study lie within, or close to the peridotite field from Sobolev et al. (2007). Additionally, they clearly lie at more peridotic values than the results of Soager et al. (2015b), despite showing significantly higher isotopic enrichment. While in b), the samples of Soager et al. (2015b) trend towards the pyroxenite field of Sobolev et al. (2007), in a) and c) they do not.

References

Roeder, P.L. and Emslie, R., 1970. Olivine-liquid equilibrium. Contributions to mineralogy and petrology, 29(4), pp.275-289.